LMEC-70-21
General, Miscellaneous,
and Progress Reports

Examination of 2-¼ Cr - 1 Mo Ferritic Steel Tubes Exposed to Small Leaks of Water in Flowing Sodium

By
W. T. Lee

This report was prepared as an account of work sponsored by the United States Government. Neither the United States nor the United States Atomic Energy Commission, nor any of their employees, nor any of their contractors, subcontractors, or their employees, makes any warranty, express or implied, or assumes any legal liability or responsibility for the accuracy, completeness or usefulness of any information, apparatus, product or process disclosed, or represents that its use would not infringe privately owned rights.

Liquid Metal Engineering Center

Operated for
the U.S. Atomic Energy Commission by Atomics International
A Division of North American Aviation, Inc

This document is
PUBLICLY RELEASABLE
Larry E. Williams
Authorizing Official
Date: 06/08/2006

Contract: AT(04-3)-700

Issued: FEB 1 1971

DISTRIBUTION OF THIS DOCUMENT IS UNLIMITED

DISCLAIMER

This report was prepared as an account of work sponsored by an agency of the United States Government. Neither the United States Government nor any agency Thereof, nor any of their employees, makes any warranty, express or implied, or assumes any legal liability or responsibility for the accuracy, completeness, or usefulness of any information, apparatus, product, or process disclosed, or represents that its use would not infringe privately owned rights. Reference herein to any specific commercial product, process, or service by trade name, trademark, manufacturer, or otherwise does not necessarily constitute or imply its endorsement, recommendation, or favoring by the United States Government or any agency thereof. The views and opinions of authors expressed herein do not necessarily state or reflect those of the United States Government or any agency thereof.

DISCLAIMER

Portions of this document may be illegible in electronic image products. Images are produced from the best available original document.

DISTRIBUTION

This report has been distributed according to the category "General, Miscellaneous, and Progress Reports" as given in "Standard Distribution Lists for Unclassified Scientific and Technical Reports," TID-4500.

ACKNOWLEDGMENT

The author wishes to acknowledge the contributions of R. K. Wagner, R. W. Perry, and K. L. Adler for their helpful discussions during the course of this work.

CONTENTS

		Page
	Abstract	7
I.	Introduction	9
II.	Experimental Procedures	13
	A. Dimensional Measurements	13
	B. Metallographic Sample Preparation	13
III.	Results	15
	A. Extent of Material Wastage	15
	B. Metallographic Data	15
	C. Scanning Electron Microscopic Data	17
	D. Hardness	21
IV.	Discussion	31
	A. Extent of Material Wastage	31
	B. Nature of Wastage	31
	C. Effect of Shock Loading on Material	37
	1. Dynamics of Shock-Loading Due to Water Impingement	37
	2. Effect of Shock-Loading on Fe and Fe Alloys	39
	3. Effect of Shock Loading on APDA Target Tubes	44
	D. Effect of Temperature Rise	47
	1. Wastage of Secondary Tubes	47
	2. Effect of Tube Location on Wastage	49
	3. Effect of Temperature on Erosion Resistance of 2-1/4 Cr - 1 Mo Steel	51
	E. Mechanism of Wastage	55
V.	Conclusions	59
	References	61
	Appendix — Macrographs of Wastage Areas of Tubes	63

TABLES

		Page
1.	Test Conditions and Data Summary for APDA Samples	11
2.	Wastage Data for Sodium-Water Reaction Target Tubes	16
3.	Comparison of Hardness Change in Primary Impact Target Tubes and in Secondary (Adjacent) Tubes	28
4.	Wastage Data for 15 Primary Target Tubes	32
5.	Effect of Shock Pressure on the Calculated Temperature at Pressure	43

FIGURES

1.	Elevation Cross Section of Tube Bundle Assembly, Rig 10	10
2.	Impact Craters, Typical of Surfaces in Wastage Areas	17
3.	Microstructure of a Target Tube (Tube 47) – Bainitic Structure with Large Proeutectoid Ferrite Grains in the Wastage Areas	18
4.	Microstructure of the Wastage Area in a Secondary Tube	19
5.	Microstructure of a Secondary Tube in the Region 180 Degrees Away from the Wastage	20
6.	Macrograph of Tube 47A-2 at the Tip of the Penetration Region	21
7.	Scanning Electron Micrographs of Region A (Figure 6) at Various Magnifications	22
8.	Scanning Electron Micrographs of Impact Areas in Region B (Figure 6)	23
9.	Scanning Electron Micrographs of Impact Areas in Region C (Figure 6)	24
10.	Scanning Electron Micrographs of Impact Areas of Maximum Wastage in Tube 48B – Low Area, Region A	25
11.	Scanning Electron Micrographs of Impact Areas in Region B (Figure 10) of Tube 48B	26
12.	Scanning Electron Micrographs of Impact Areas in Region C (Figure 10) of Tube 48B	26
13.	Scanning Electron Micrographs of the Impact Area in Tube TR50	27
14.	Impingement Damage on Tube TR45 (Primary Target Tube) Showing a Toroidal Wastage Pattern	28
15.	Scanning Electron Micrographs of Region A (Figure 14) for Tube TR45	29

FIGURES

Page

16. Scanning Electron Micrographs of Region B (Figure 14) for Tube TR45 30
17. Effect of Water Injection Rate on Primary Target-Tube Wastage Rate 33
18. Effect of Water Injection Rate on Volume Wastage Rate 34
19. Typical Micrographs of the Outside Diameter Surfaces in Wastage Areas 35
20. Macrograph of Tube TR47A-2 (Secondary Tube) Showing the Thin Wastage Areas, A and B, and the Areas 180 Degrees Away from the Wastage, C 36
21. Transient Impact Pressure on a Steel Target as a Function of Water Droplet Velocity 39
22. Hugoniot Curve for Iron 41
23. Variations of Transition Pressures with Ni and Cr Content in Iron Alloys 41
24. Hugoniot Curves for Iron-Chromium Alloys 41
25. Effect of Cold Rolling on Twinning by Shock Loading 42
26. Distribution of Twins Oriented at Various Angles to the Specimen Surface in Iron after Pressing in Liquid Nitrogen and After Shock Loading to 500 kbars 42
27. Hardness vs Shock Pressure for Iron 44
28. Effect of Test Temperature on the Critical Resolved Shear Stress τ_Y for Slip and Twinning in a Typical BCC Metal 46
29. Continuous-Cooling Transformation Diagram for 2-1/4 Cr - 1 Mo Steel 48
30. Hypothetical Variation of Temperature with Distance Traveled by Droplet/Jet 52
31. Hypothetical Variation of Mean Velocity of Jet of Droplets with Distance Traveled 52
32. Effect of Temperature on Tensile Strength of 2-1/4 Cr - 1 Mo Ferritic Steel 53
33. Hot Microhardness Data for a Ferritic Steel 53
34. Variation of Calculated Strain Energy with Temperature for 2-1/4 Cr - 1 Mo Ferritic Steel 54
35. Variation of Ultimate Resilience with Temperature for 2-1/4 Cr - 1 Mo Ferritic Steel 54
36. Idealized Configuration of the Droplet Impingement and Sodium-Water Reaction Processes in Rig 10 56

ABSTRACT

Metallurgical examinations and evaluations were performed on a group of 52 2-1/4 Cr - 1 Mo ferritic steel target tubes from Atomic Power Development Associates' Rig 10. These tubes were exposed to small leaks of water in 600°F flowing sodium. The extent of wastage was determined by dimensional and volumetric measurements. Metallographic, hardness, and scanning electron microscopic analyses indicate that the tube wastage process was controlled by (1) droplet impingement, and (2) temperature rise in the target tube caused by sodium-water reaction. A probable mechanism of wastage for the tubes is postulated.

I. INTRODUCTION

Fifty-two tubes [tested under the Atomic Power Development Associates (APDA) Sodium-Water Reaction Program] were received from APDA for metallurgical examination and evaluation. All the tubes were made of nominal 2-1/4 Cr - 1 Mo ferritic steel with 1-in. OD. The distributions of the primary target tube and of the secondary tubes in the test assembly (Rig 10) are displayed in Figure 1. The nominal wall thickness of the tubes in row A was 1/16 in., in rows B and C it was 1/8 in. The target tubes were exposed to water-jet impingement and sodium-water reaction in APDA's Rig 10. The test conditions and results are summarized in Table 1.[1]

The objective of this evaluation is to characterize the nature of wastage damage of the primary and secondary tubes. The scope of work included:

1) Measurement of the extent of erosion and/or corrosion.

2) Determination of the nature and mechanism of wastage.

3) Determination of the maximum temperature reached by the affected material in the wastage areas.

4) Determination of the contribution to plastic straining due to water-jet impact and subsequent thermal surge resulting from sodium-water reaction and/or impact.

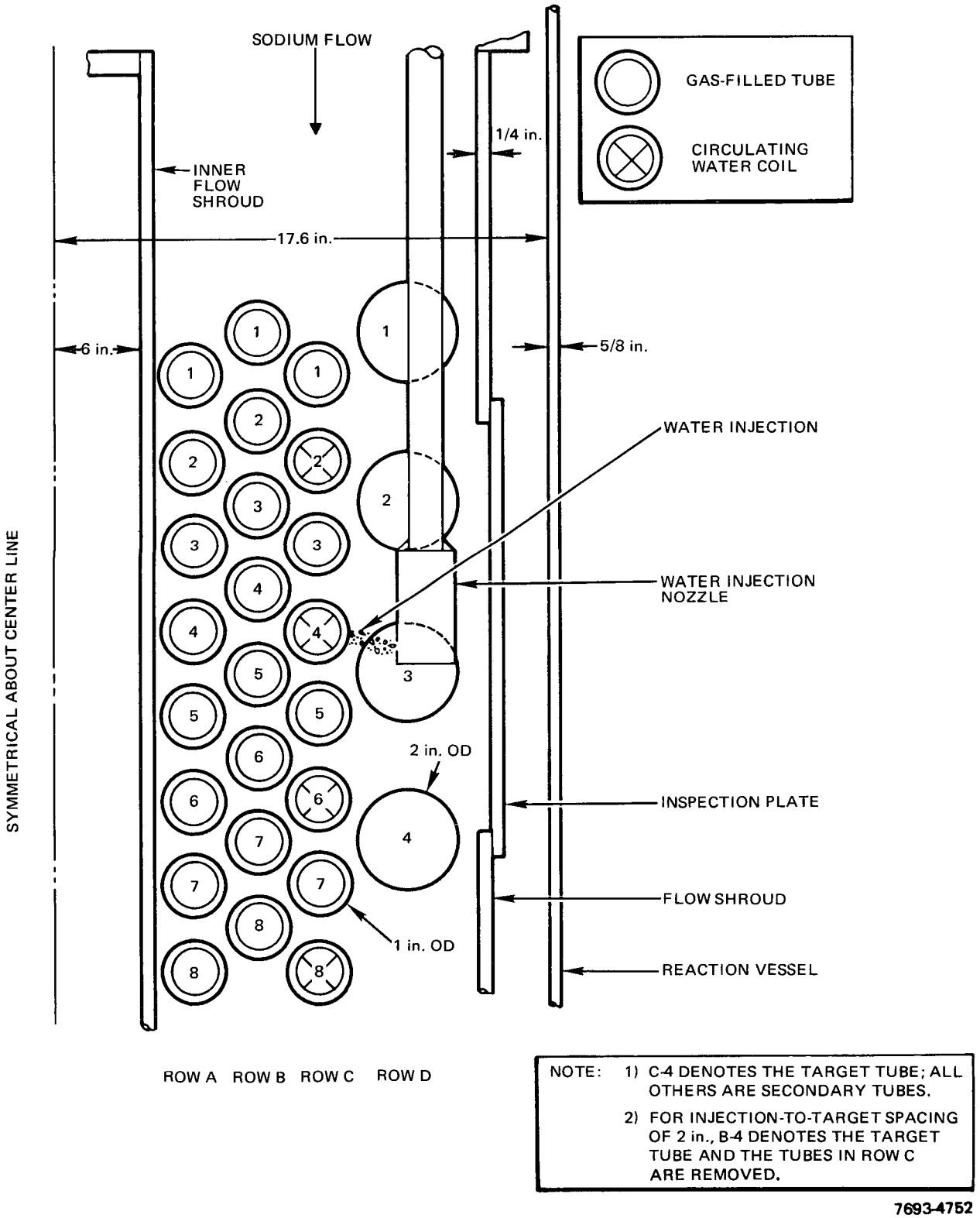

Figure 1. Elevation Cross Section of Tube Bundle Assembly, Rig 10[1]

TABLE 1

TEST CONDITIONS AND DATA SUMMARY FOR APDA SAMPLES[1]
(Target Material — 2-1/4 Cr - 1 Mo Steel)

Test Conditions	Test Number/Date														
	40	41	42	43	44	45	46	47	48	48(a)	48(b)	50	51	52	53
	3-27-69	5-3-69	5-9-69	6-6-69	5-19-69	8-1-69	11-20-69	10-30-69	8-29-69	9-12-69	10-14-69	9-25-69	12-11-69	2-4-70	2-17-70
Na System															
Flowrate (gpm)	400	400	400	400	400	400	400	400	400	400	400	400	400	400	400
Na velocity (fps)	2	2	2	2	2	2	2	2	2	2	2	2	2	2	2
Bulk temperature (°F)	615	617	600	610	585	602	600	610	600	600	603	605	606	600	610
Injection Water System															
H_2O added (lb)	0.22	2	10	20	2	0.30	10	20	0.24	0.24	0.24	1.0	20	10	20
Temperature (°F)	615	617	600	600	585	602	600	610	600	600	603	605	606	600	600
Pressure (psig)	2650	2650	2650	2650	2650	2650	2650	2650	2650	2650	2650	2650	2650	2650	2650
Orifice size (in.)	0.012	0.036	0.085	0.128	0.038	0.012	0.043	0.062	0.009	0.009	0.008	0.02	0.059	0.043	0.085
Injection spacing (in.)	1.0	1	1	1	1	1/4	1/4	1	1/4	1/4	1/4	1	1	2	2
Injection duration (sec)	24.5	28	16	11.5	14.5	32.6	50	62.5	762	11,040	55	42	59.5	43	25
Injection rate (lb/sec)	0.009	0.071	0.63	1.7	0.071	0.009	0.20	0.32	0.0003	0.00002	0.004	0.024	0.34	0.23	0.79
Target Tube															
Fluid in tube	Stagn. N_2	Stagn. N_2	Stagn. N_2	Stagn. N_2	H_2O	Stagn. N_2	Stagn. N_2	Stagn. N_2	Stagn. N_2	Stagn. N_2	Stagn. N_2	Stagn. N_2	Stagn. N_2	Stagn. N_2	Stagn. N_2
Pressure (psig)	100	100	100	100	2650	100	100	100	100	100	100	100	100	100	100
Wastage															
Pattern	*	†	-	-	§	**	§	§	**	**	**	§	-	§	§
Penetration depth (mils)	14	31	Neg.	Neg.	14	18	15	4	17	2	20	26	12	29	11
Wastage rate (mil/sec)	0.57	1.11	-	-	0.96	0.55	0.30	0.06	0.022	0.0002	0.37	0.62	-	0.67	0.44
Maximum measured T (°F)	1380	1887	1901	ND	1749	1553	1870	1821	983	639	1444	1628	1901	1860	1930
Time of maximum T (sec)	16	3.4	15	-	4.5	18	49	61	0.6	0.05	40 & 46	36	15	26	27
Area of wastage ($in.^2$)	ND††	ND	ND	ND	ND	ND	ND	ND	ND	ND	ND	ND	ND	ND	ND
Volume of wastage ($in.^3$)	ND	ND	ND	ND	ND	ND	ND	ND	ND	ND	ND	ND	ND	ND	ND
Cover Gas Pressure															
Before triggering (psig)	6	5	5	5	5	6	5	5	5	5	9.5	5	5	6	5
Peak during test (psig)	16.5	19	20	32	12	12	15	19	-	-	11	14	20	20	25

*Broad, shallow depression
†Shallow pit
§Large area, central hump
**Shallow pit
††ND - No data

II. EXPERIMENTAL PROCEDURES

A. DIMENSIONAL MEASUREMENTS

The extent of erosion/corrosion was determined by dimensional and volumetric measurements. Dimensional measurements (maximum length, width, and depth of the impact area) were made from Facsimile* castings of the indented areas by using a Scherr microprojector (precision ±0.001 in.). Volume of the affected areas was measured from impressions of the idented areas. Facsimile was used because of its ease of application and its accurate dimensional reproducibility.[2]

Castings were made at room temperature and were shaped (filed) at room temperature to match the contour of the tubes. Dimensional accuracy was checked and assured by a Scherr microprojector. After the castings were made, the volume of wastage was measured at room temperature by immersing the Facsimile impression in a 10-cc burette, 10- or 30-cc graduated cylinder (depending on the size of the casting), containing a known level of water. The net volume of the wastage area was determined by fluid displacement in the burette or in the graduated cylinder.

B. METALLOGRAPHIC SAMPLE PREPARATION

After being sectioned, the samples were mounted for metallography and hardness measurements. Normal procedures were used for the metallographic sample preparation. Nital etchant (95% HNO_3 + 5% methanol) was used for all the samples. Microhardness testing was done on a standard Leitz Miniload hardness tester with 100-gm load. Hardness identations were made on wastage areas as well as on areas 180 deg away from wastage. In some cases, detailed hardness indentations were made in selected areas of the impact region for comparison.

*Trade name of a plastic material made especially for the duplication of surface roughness and indentation.

III. RESULTS

A. EXTENT OF MATERIAL WASTAGE

The extent of material wastage due to impingement/erosion was determined by dimensional and volumetric measurements. Wastage (indented) areas of sufficient size to measure were found on only 21 of 52 tubes. The results are shown in Table 2.

B. METALLOGRAPHIC DATA

Macrographs of the impact areas were taken for the 21 tubes which exhibited measurable indentation on the tube surface. The results are presented in the Appendix. In general, the surfaces in the wastage areas appeared to be polished and somewhat shiny.

Stereomicroscopic examination of the impacted areas revealed irregular indented surfaces with a high density of impingement craters. Typical impingement craters are shown in Figure 2. The hemispherical craters are particularly evident in areas away from the region of highest wastage, which, in general, exhibited a polished and smooth appearance.

Microstructural examination of the primary target tubes (e.g., TR44, TR46, TR47, and TR52-B4) disclosed a general bainitic structure with large, proeutectoid ferrite grains (Figure 3), a microstructure typical of normal 2-1/4 Cr - 1 Mo ferritic steel. In addition to the presence of undissolved carbides in the ferrite grains, retained austenite (identified by selective etching) was found in the tube. No mechanical twinning bands or Neumann bands were detected in the ferrite grains. Special effort was devoted to detect the presence of recrystallization, but no such indication was found. Furthermore, no indication of corrosion was observed in the wastage areas.

Microstructural examination of the wastage areas in the secondary tubes (e.g., TR47-A2, TR47-A3, TR46-B3-A) revealed a significantly different structure relative to the primary target tubes. Specifically, the wastage areas in the secondary tubes exhibited a coarse bainite structure with practically no proeutectoid ferrite grains (Figure 4). The second-phase particles (retained austenite) appeared to have increased and their distribution appeared to be random

TABLE 2

WASTAGE DATA FOR SODIUM-WATER REACTION TARGET TUBES

Sample No.	Depth (in.)	Volume (cc)	Length (in.)	Width (in.)	Sample No.	Depth (in.)	Volume (cc)	Length (in.)	Width (in.)
40	0.017 ± 0.002	0.10 ± 0.00	0.43	0.59	48-	0.015 ± 0.001	0.02 ± 0.00	0.61	0.49
41	0.041 ± 0.001	0.38 ± 0.03	1.81	1.14	48(a)	-	-	-	-
41-B3	-	-	-	-	48(b)	0.026 ± 0.00	0.08 ± 0.01	0.04	0.09
41-B5	-	-	-	-	50-	0.023 ± 0.001	0.22 ± 0.02	1.29	1.03
42	-	-	-	-	51-	-	-	-	-
43	-	-	-	-	51-C1	-	-	-	-
44	0.043 ± 0.001	0.55 ± 0.20	0.58	0.76	51-C2	-	-	-	-
44-B5	-	-	-	-	51-C3	-	-	-	-
45	0.044 ± 0.001	0.30 ± 0.00	2.36	1.45	51-C5	-	-	-	-
46	0.020 ± 0.001	0.90 ± 0.06	3.52	1.50	51-C6	-	-	-	-
46-A2	-	-	-	-	52-A2	-	-	-	-
46-A3	0.021 ± 0.001	0.37 ± 0.03	2.52	0.94	52-A3	0.035 ± 0.001	1.97 ± 0.01	6.15	1.78
46-A4	-	-	-	-	52-A4	0.009 ± 0.001	0.60 ± 0.0	2.93	1.83
46-A5	-	-	-	-	52-A5	-	-	-	-
46-A6	-	-	-	-	52-B3	-	-	-	-
46-B2	-	-	-	-	52-C4	-	-	-	-
46-B3	0.039 ± 0.001	1.27 ± 0.012	3.21	0.24	52-B4	-	-	-	-
46-B4	0.031 ± 0.002	0.05 ± 0.001	1.73	0.81					
46-B5	0.017 ± 0.001	0.97 ± 0.18	4.95	1.96	53-B4	-	-	-	-
46-B6	-	-	-	-	53-A3	-	-	-	-
46-C2	-	-	-	-	53-A4	-	-	-	-
46-C5	-	-	-	-	53-A5	0.016 ± 0.001	0.33 ± 0.018	2.0	1.31
47-	0.013 ± 0.001	0.03 ± 0.001	0.60	0.51	53-B3	-	-	-	-
47-A2	0.068 ± 0.003	1.62 ± 0.17	4.03	0.67	53-B5	-	-	-	-
47-A3	0.065 ± 0.002	1.45 ± 0.003	4.52	1.26	53-C4	-	-	-	-
47-B3	0.022 ± 0.001	0.12 ± 0.001	1.25	0.71					
47-B5	0.025 ± 0.001	0.90 ± 0.0	3.35	1.58					
47-C5	0.035 ± 0.001	0.87 ± 0.04	3.71	1.80					

Note: - denotes that the impact areas were too shallow to be measured.

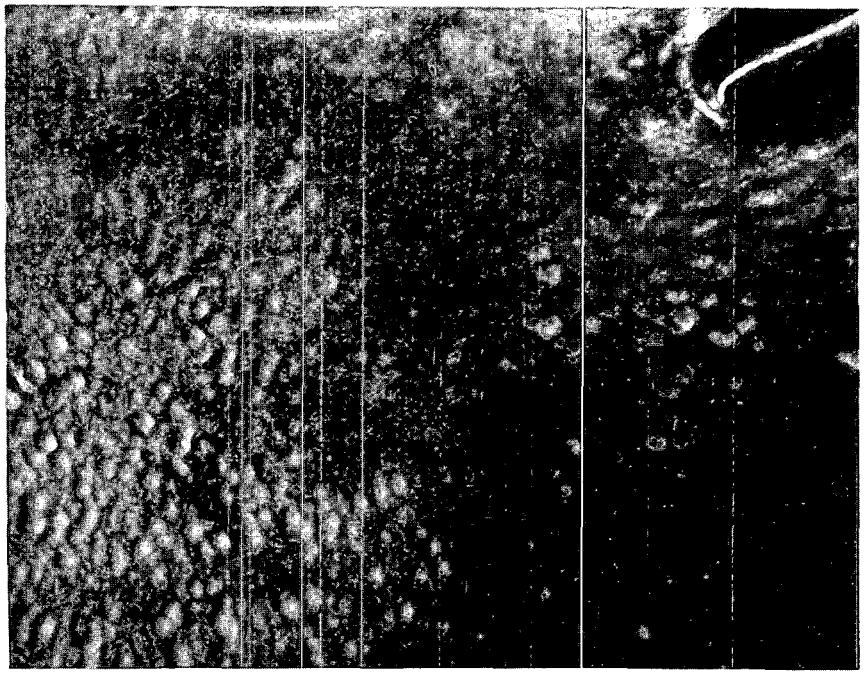

Mag 10X 7693-4753

Figure 2. Impact Craters, Typical of Surfaces in Wastage Areas

in the grain. However, in areas 180 deg away from wastage, the proeutectoid ferrite grains were again apparent in the bainitic structure, as shown in Figure 5. Again, no twinning bands or Neumann bands were found in the ferrite grains. No indication of corrosion was observed in the wastage areas.

C. SCANNING ELECTRON MICROSCOPIC DATA

Four sections (1/2 x 1/2 x 1/8 in.) of the wastage areas from four different target tubes (TR47-A2, TR48-B, TR50, and TR45) were cleaned and examined under a scanning electron microscope. The results are shown in Figures 6 through 16. In addition to those large craters observed under an optical microscope (Figure 2), a large number of microcraters in the size range of 1 to 2 microns was found in the wastage areas.

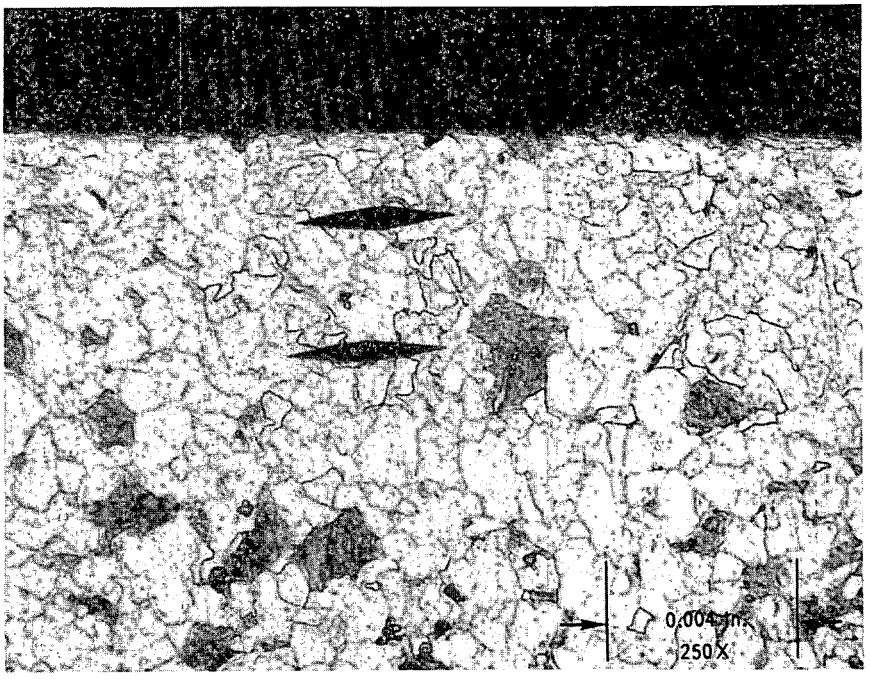

a. Microstructure at Outside Diameter

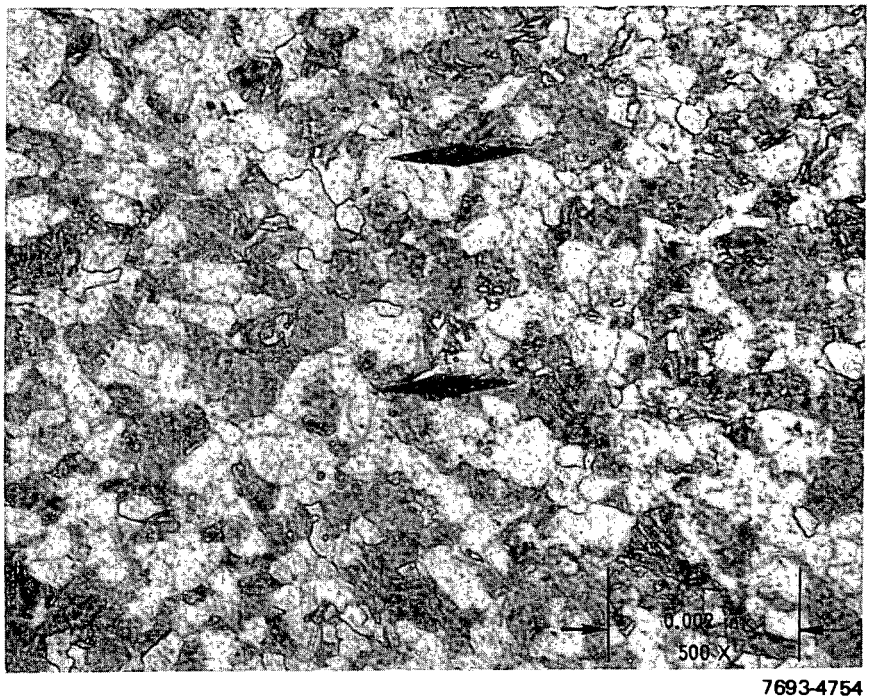

7693-4754

b. Microstructure at the Middle of the Tube Wall

Figure 3. Microstructure of a Target Tube (Tube 47) — Bainitic Structure with Large Proeutectoid Ferrite Grains in the Wastage Areas

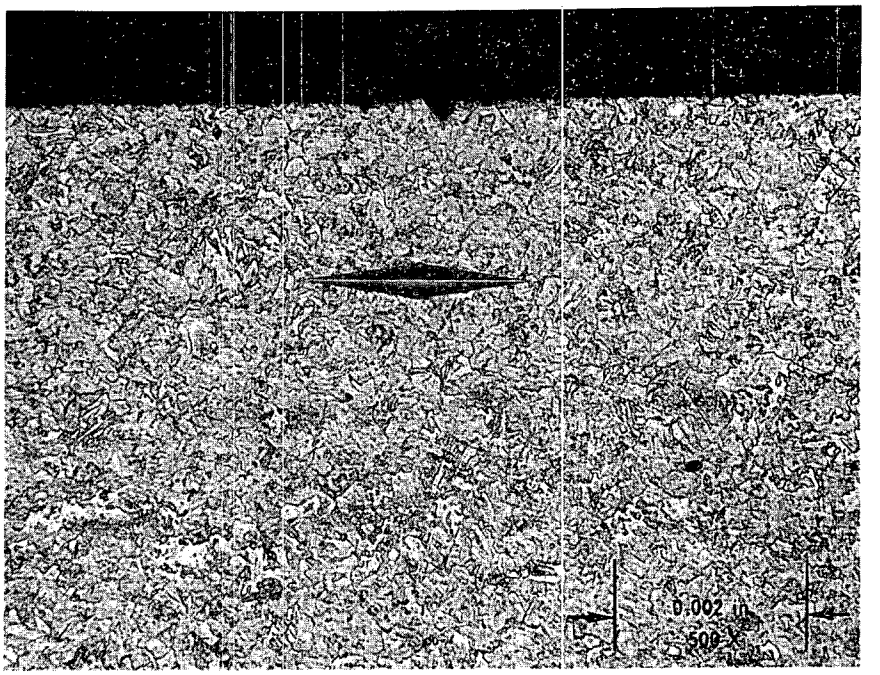

a. Outside Diameter of the Wastage Area

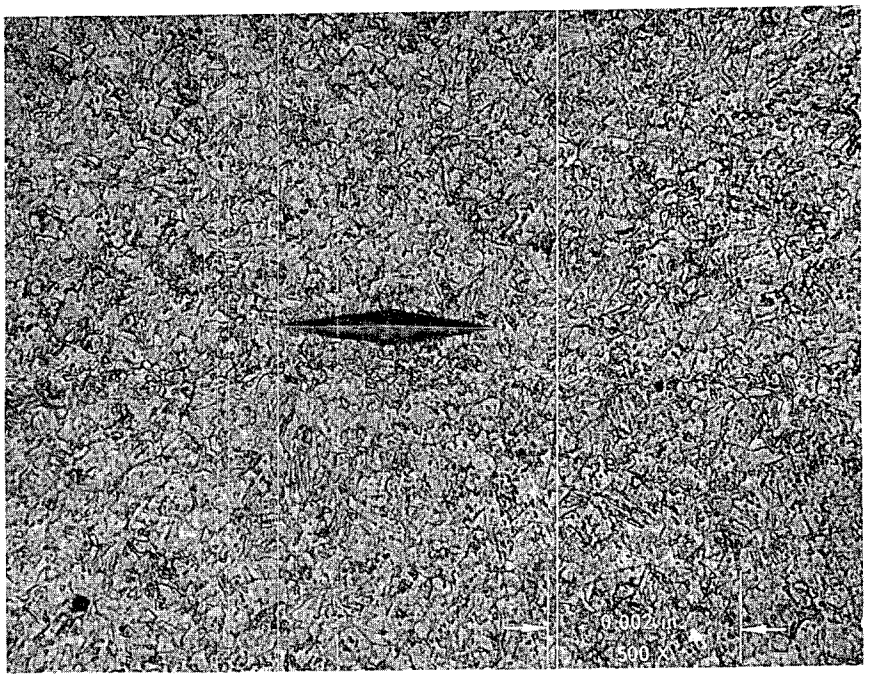

7693-4755

b. Mid-Wall of Tube

Figure 4. Microstructure of the Wastage Area in a Secondary Tube — Note the Virtual Absence of Large Proeutectoid Ferrite Grains

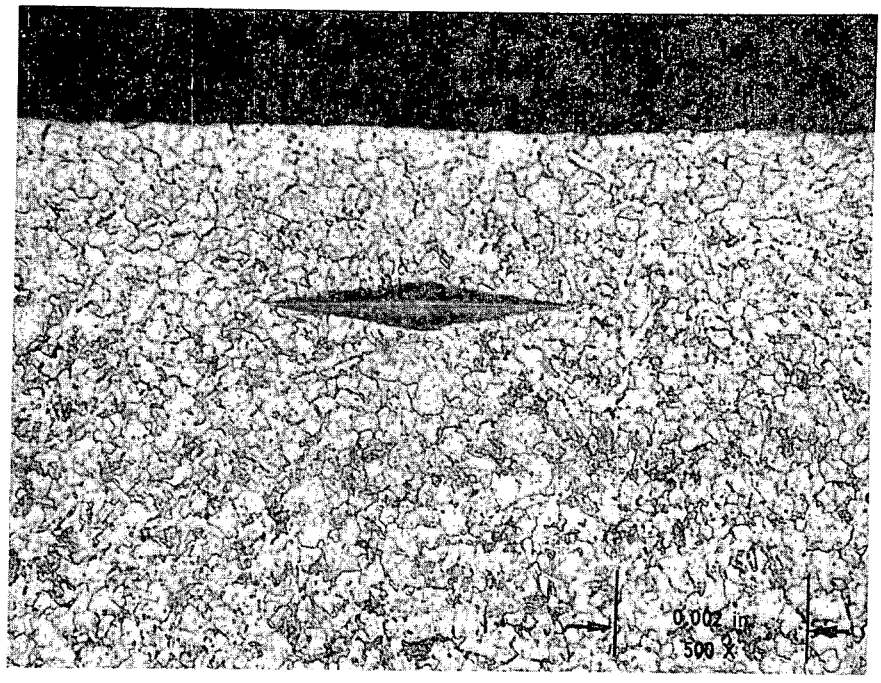

a. Outside Diameter of Tube

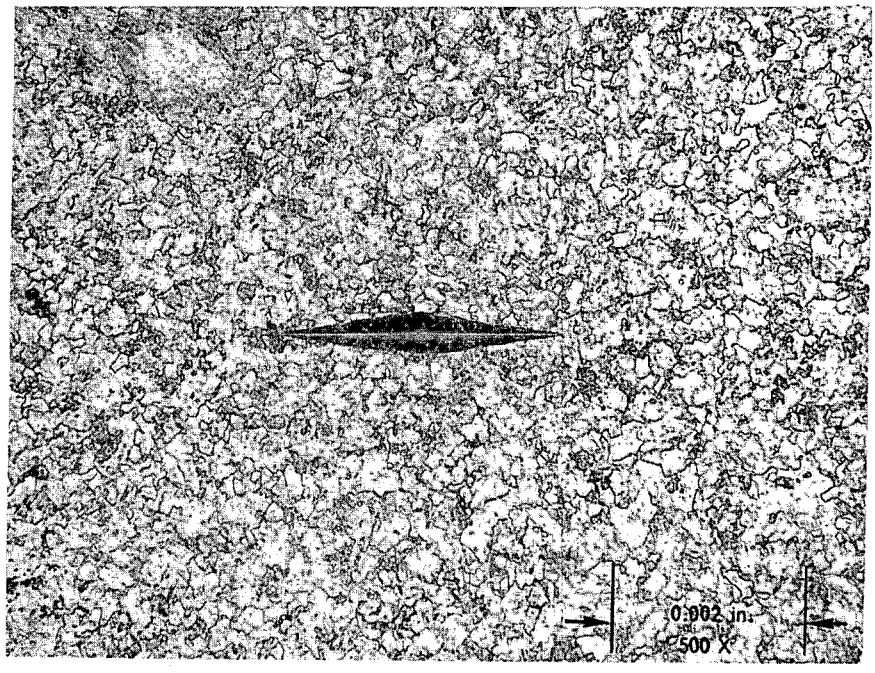

7693-4756

b. Mid-Wall of Tube

Figure 5. Microstructure of a Secondary Tube in the Region 180 Degrees Away from the Wastage — Note the Presence of Large Proeutectoid Ferrite Grains and Bainite Structure

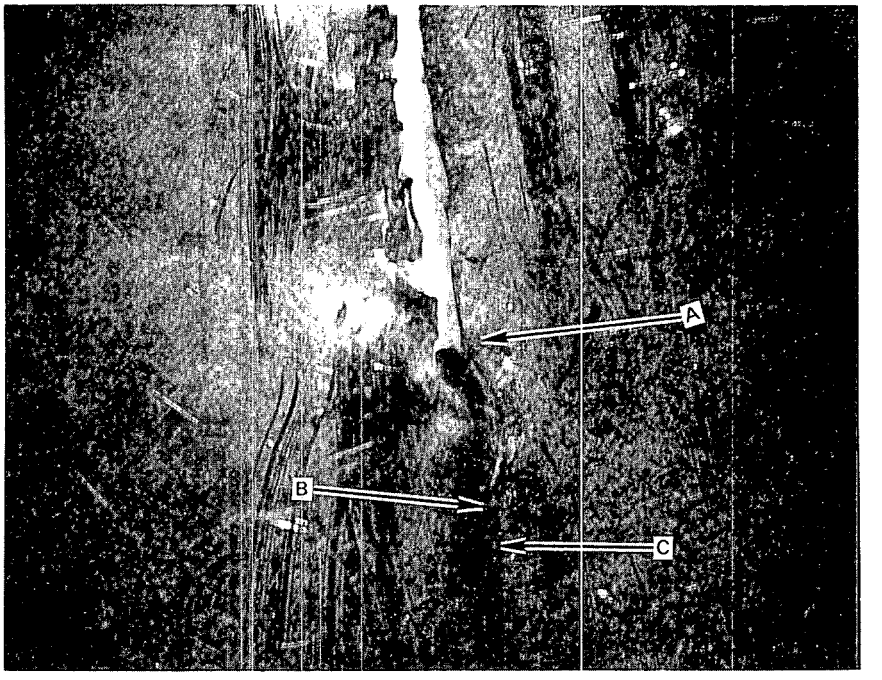

(Mag 10X) 7693-4757

Figure 6. Macrograph of Tube 47A-2 at the Tip of the Penetration Region. Regions A, B, and C Correspond to Top, Tip, and Bottom, Respectively, of the Sections Traversed by the Scanning Electron Microscope

D. HARDNESS

Hardness measurements were made on five primary target tubes and six secondary tubes. The average hardness values of the tubes are shown in Table 3 which shows that there is a significant difference between the hardness values in the primary target tubes and the secondary tubes. Specifically, in the primary target tubes, there is no difference in hardness between the impact area and the area 180 deg away from impact. However, for secondary or adjacent tubes, there is a significant difference in hardness (maximum change of hardness is ~200 KHN, Knoop Hardness Number) between the wastage areas and areas 180 deg away from the wastage. For example, the average hardness in the wastage area is 391 KHN for tube TR47-A2; and the average hardness values in areas 180 deg away from wastage is only 228 KHN. As shown in Table 3, there is no difference in hardness between the wastage area and the area 180 deg away from wastage for tube TR46-A2. But it should be noted that tube 46-A2 also showed no measurable wastage.

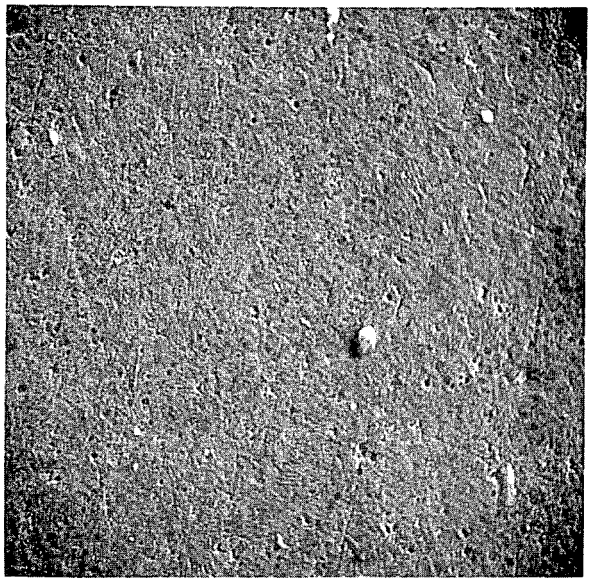

(Mag 700X)

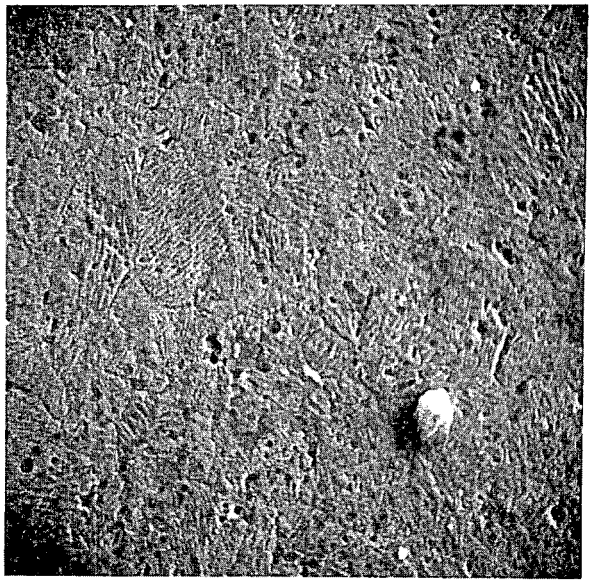

(Mag 1400X)

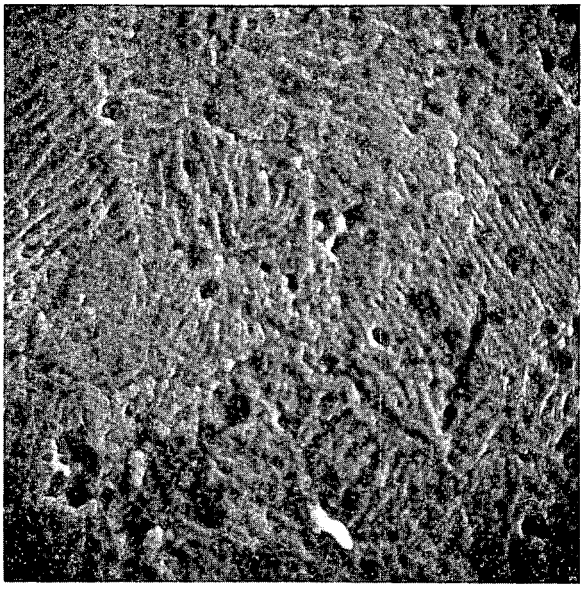

(Mag 3500X)

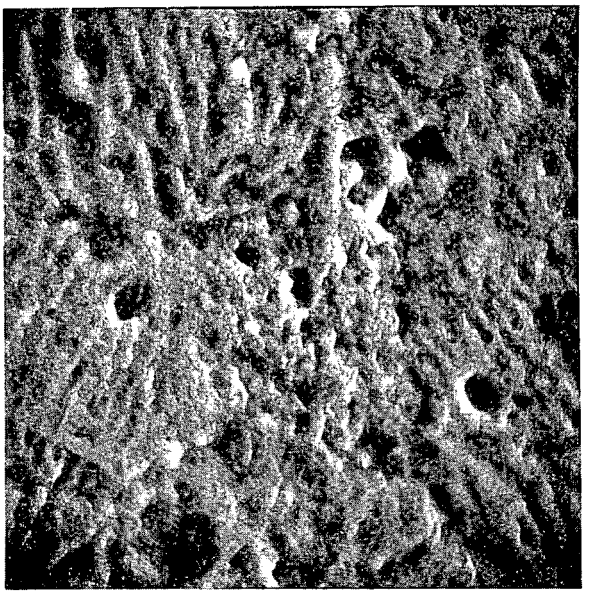

(Mag 7000X)

7693-4758

Figure 7. Scanning Electron Micrographs of Region A (Figure 6) at Various Magnifications — Secondary Tube

(Mag 1400X)

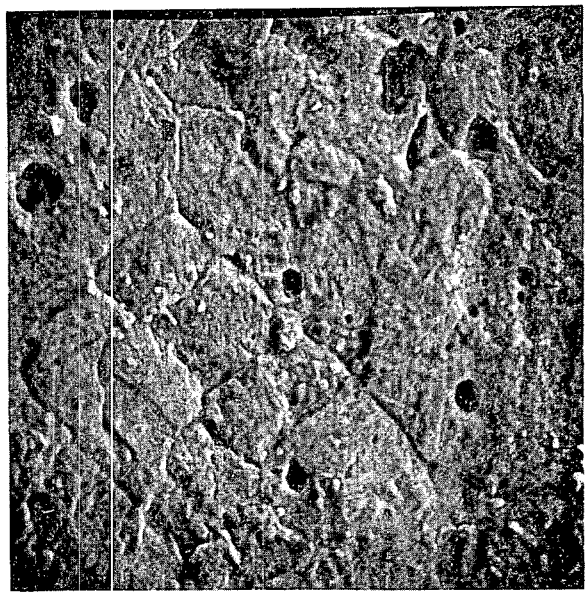

(Mag 3500X)

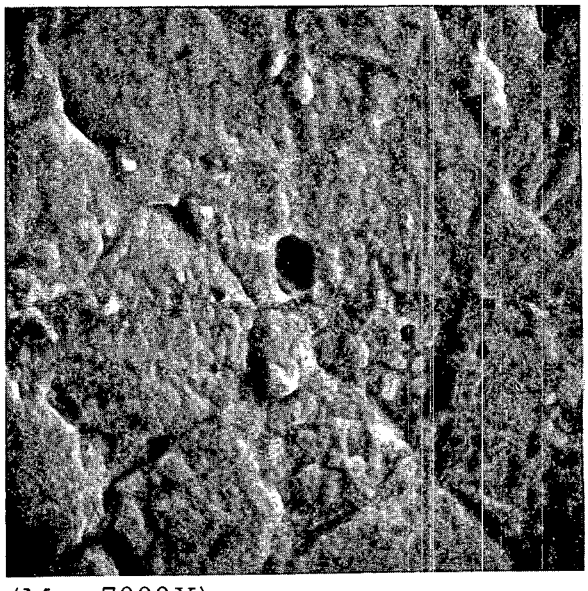

(Mag 7000X)

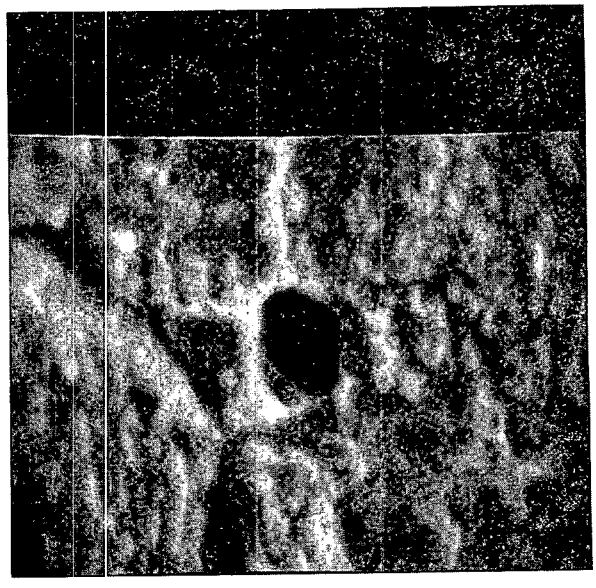

(Mag 14,000X)

7693-4759

Figure 8. Scanning Electron Micrographs of Impact Areas in Region B (Figure 6) — Microcraters Probably Produced by Impingement (Secondary Tube)

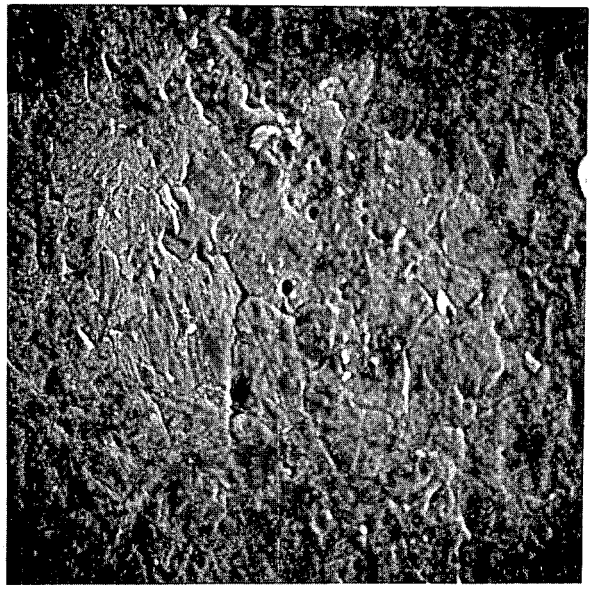

(Mag 700X)

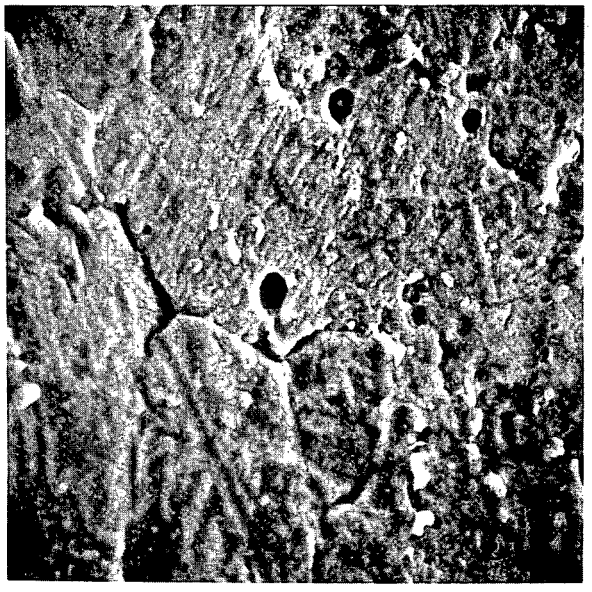

(Mag 3500X) 7693-4760

Figure 9. Scanning Electron Micrographs of Impact Areas in Region C (Figure 6) – Microcraters Probably Produced by Particles Impingement (Secondary Tube)

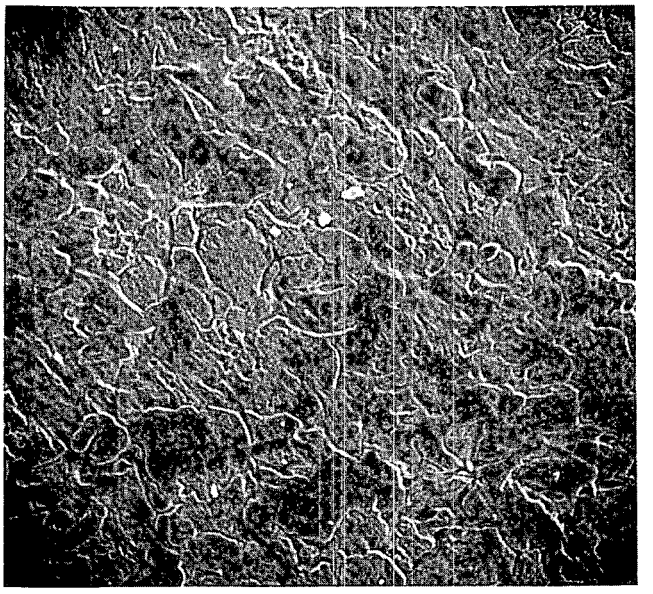

(MAG 350X)

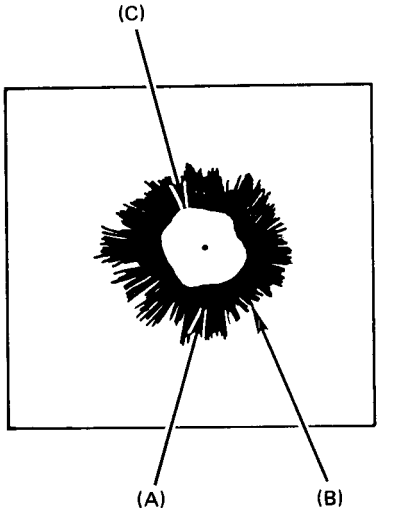

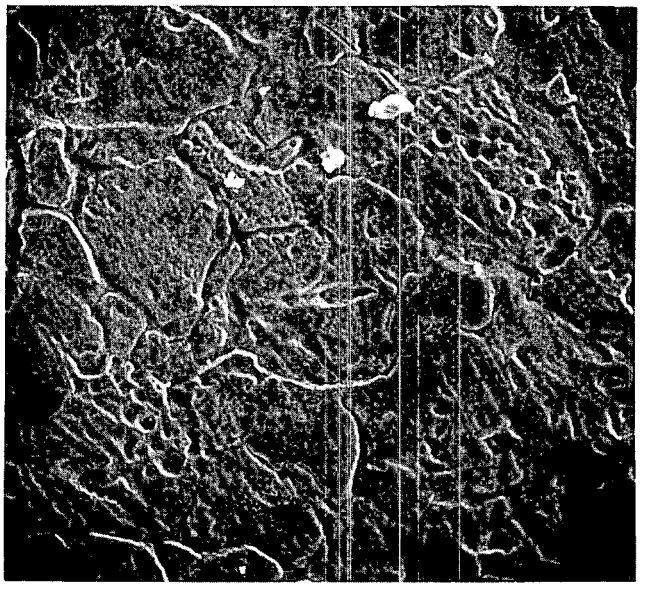

(MAG 700X)

7693-4761

Figure 10. Scanning Electron Micrographs of Impact Areas of Maximum Wastage in Tube 48B – Low Area, Region A – Primary Target Tube

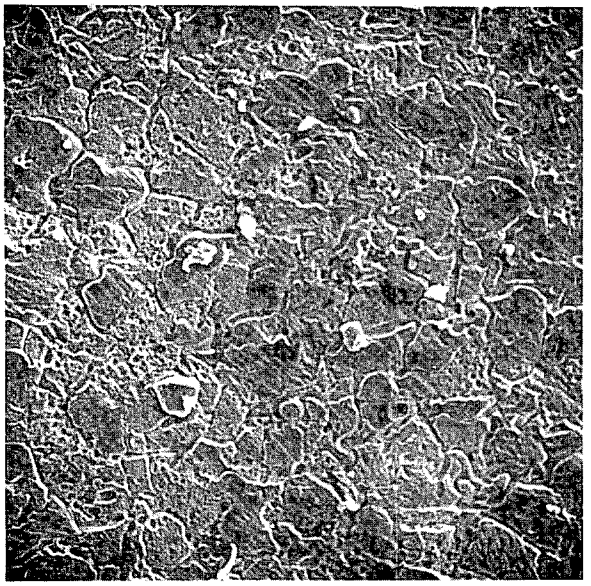

(Mag 350X)

(Mag 700X) 7693-4798

Figure 11. Scanning Electron Micrographs of Impact Areas in Region B (Figure 10) of Tube 48B – Primary Target Tube

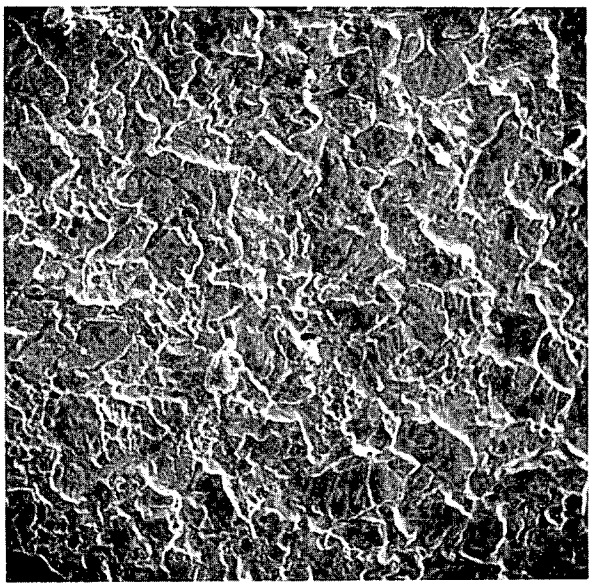

(Mag 350X)

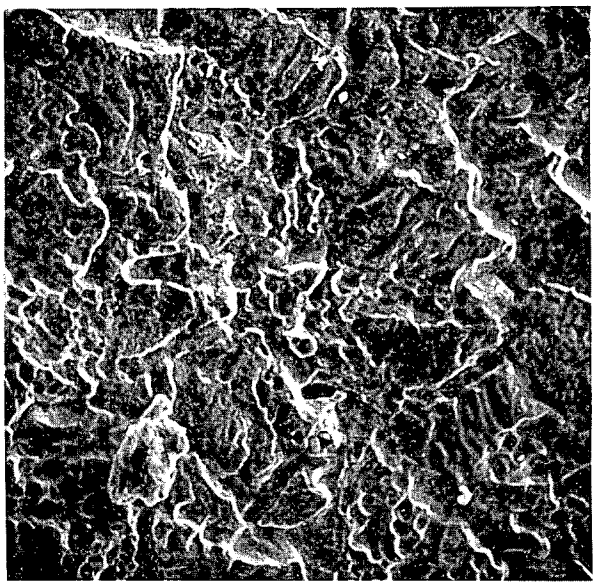

(Mag 700X) 7693-4762

Figure 12. Scanning Electron Micrographs of Impact Areas in Region C (Figure 10) of Tube 48B – Primary Target Tube

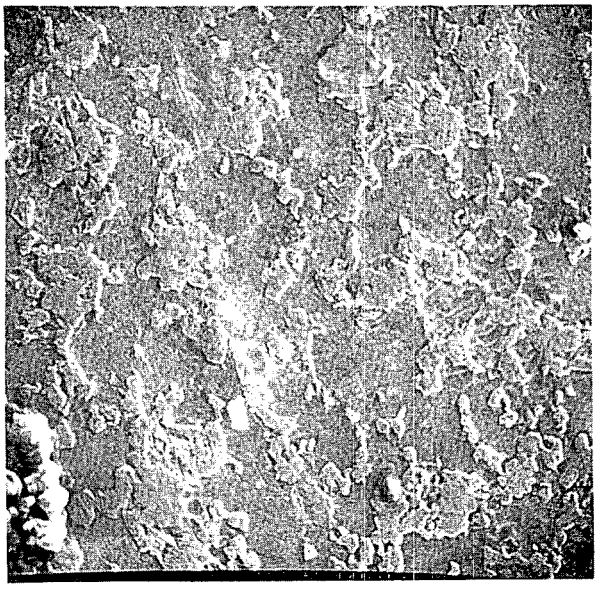

(Mag 350X)

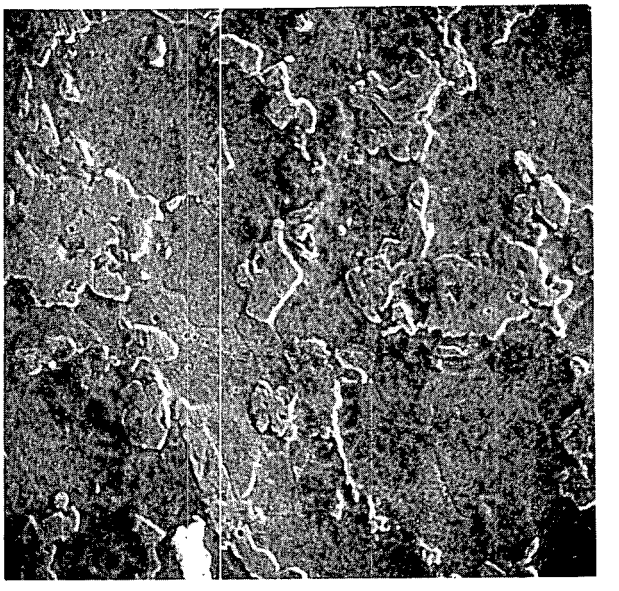

(Mag 700X) 7693-4763

Figure 13. Scanning Electron Micrographs of the Impact Area in Tube TR50 — Primary Target Tube

TABLE 3

COMPARISON OF HARDNESS CHANGE IN PRIMARY IMPACT TARGET TUBES AND IN SECONDARY (ADJACENT) TUBES

Primary Impact Target Tubes			Secondary (Adjacent) Tubes		
Tube No.	Average Hardness (KHN)		Tube No.	Hardness (KHN)	
	Impact Area	180 deg Away from Impact		Wastage Area	180 deg Away from Wastage
TR41	429	445	TR46-A2	154*	169
TR44	233	214	TR46-B3A	394	183
TR46	243	234	TR47-A2	391	228
TR47	233	228	TR47-A3	313	194
TR52-B4	411	429	TR47-B3	374	239
			TR52-A3	435	253

*No measurable wastage

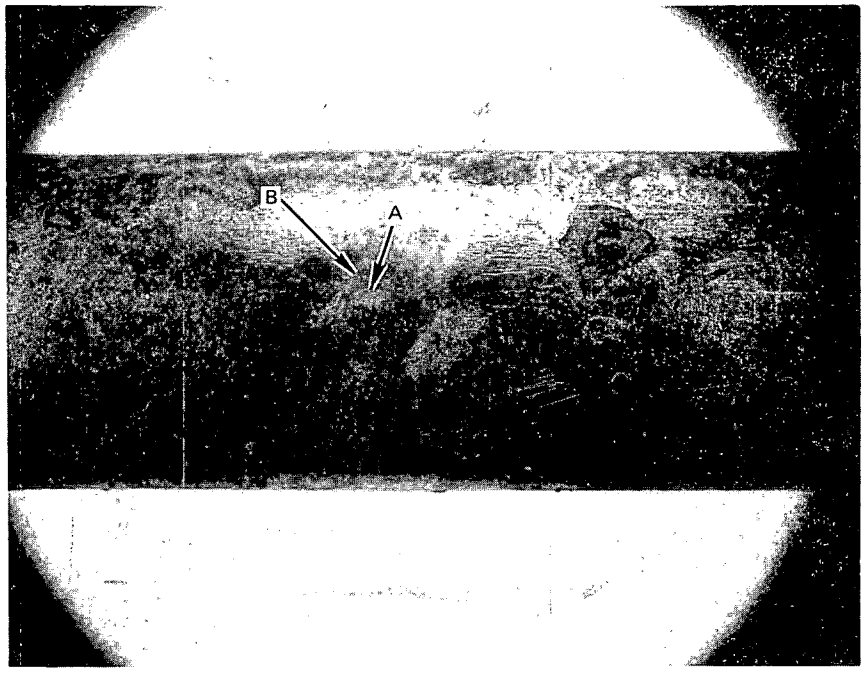

(Mag 2X) 7693-4764

Figure 14. Impingement Damage on Tube TR45 (Primary Target Tube) Showing a Toroidal Wastage Pattern

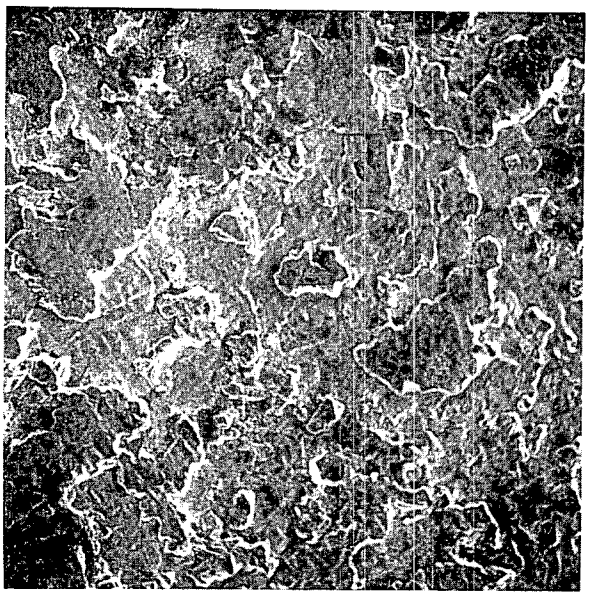

(Mag 350X)

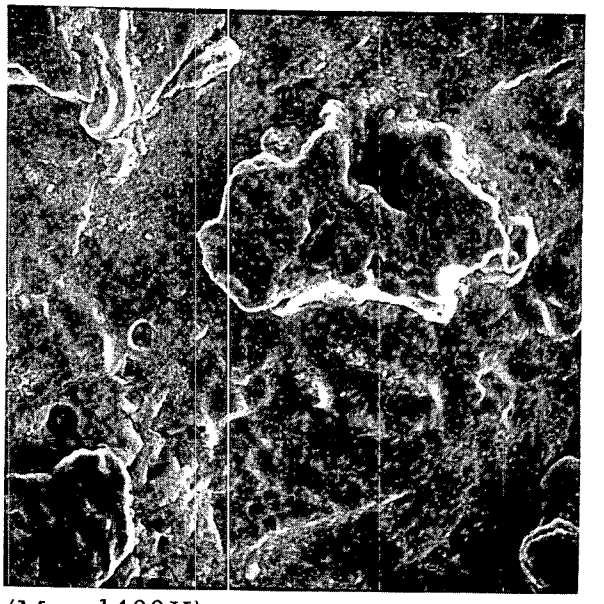

(Mag 1400X)

7693-4765

Figure 15. Scanning Electron Micrographs of Region A (Figure 14) for Tube TR45 — Primary Target Tube

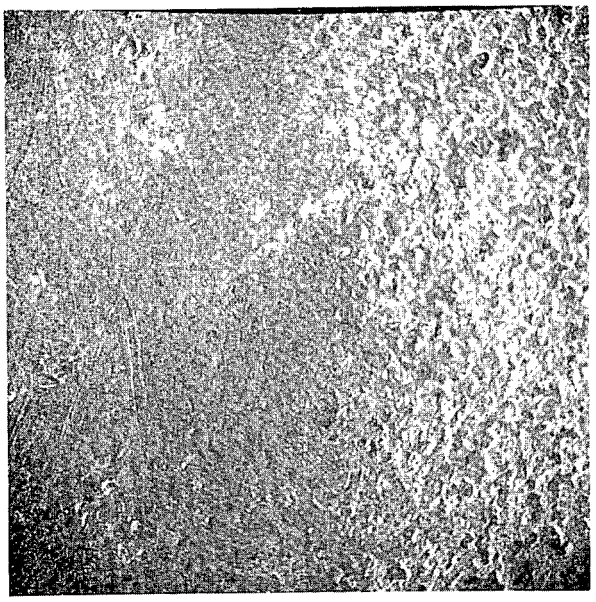

(Mag 70X)

(Mag 350X)

(Mag 700X)

7693-4766

Figure 16. Scanning Electron Micrographs of Region B (Figure 14) for Tube TR45

IV. DISCUSSION

A. EXTENT OF MATERIAL WASTAGE

The extent of material wastage (removal) due to impact and sodium-water reactions, or both, is presented in Table 2. The value presented for each tube is an average of three measurements made on three Facsimile castings for each tube. Since there are only three measurements made for each tube, the standard deviation of the mean, S_m, is used for the quoted error for each tube. The quoted error or standard deviation from the mean for each tube is also listed in Table 2. It can be seen that the depths and volumes of wastage can be reliably reproduced by the casting technique.

A comparison of the depth of penetration measurements made by LMEC and those made by APDA is shown in Table 4. No comparison was made on the volume of wastage for the target tubes because there was no comparative data available. In general, the depths of penetration measured in this investigation are somewhat higher than those obtained by APDA.

A summary of the average rates of wastage of the primary target tubes obtained in this investigation is also shown in Table 4. The effect of water injection rate on primary target tube penetration (depth) rate is plotted in Figure 17. It can be seen that the water injection rate in the range of 1×10^{-2} to 10^{-1} lb/sec appears to impart the maximum damage (penetration) on the primary target tubes. APDA data are also included for comparison purposes. However, for the rate of volume wastage (in cc/sec), this type of correlation is not found (Figure 18).

B. NATURE OF WASTAGE

For all the primary target tubes and secondary tubes examined under a light microscope (total 12 tubes), no evidence of corrosion in the indented impact areas was observed. Typical micrographs of the clean eroded outside diameter surfaces in the wastage areas are shown in Figure 19. Macroscopic evidence of mechanical damage due to droplet impingement is presented in Figure 2; typical impact craters found in wastage areas are shown. In addition, the presence of plastic straining or bending in the wastage areas is illustrated by Figure 20.

TABLE 4

WASTAGE DATA FOR 15 PRIMARY TARGET TUBES

Sample Number	Depth of Penetration (mil)		Rate of Penetration (mil/sec)		Volume Wastage (cc)	Rate of Wastage (cc/sec)	Injection Duration (sec)	Water Added (lb)	Water Injection Rate (lb/sec)	Orifice Size (in.)	Injection-to-Target-Spacing (in.)
	LMEC	APDA	LMEC	APDA							
40	17	14	0.70	0.57	0.10	4.1×10^{-4}	24.5	0.22	0.009	0.012	1
41	41	31	1.46	1.11	0.38	1.4×10^{-2}	28.0	2.0	0.071	0.036	1
42	Neg.	Neg.	-	-	Neg.	-	16.0	10.0	0.630	0.085	1
43	Neg.	Neg.	-	-	Neg.	-	11.5	20.0	1.70	0.128	1
44	43	14	2.96	0.96	0.55	3.8×10^{-2}	14.5	2.0	0.14	0.038	1
45	44	18	1.35	0.55	0.30	9.2×10^{-2}	32.6	0.3	0.009	0.012	1/4
46	20	15	0.40	0.30	0.90	1.8×10^{-2}	50.0	10.0	0.20	0.043	1/4
47	13	4	0.21	0.064	0.03	4.8×10^{-4}	62.5	20.0	0.32	0.062	1
48	15	17	0.02	0.02	0.02	2.6×10^{-5}	762.0	0.24	0.0003	0.009	1/4
48(a)	Neg.	2	-	0.0002	Neg.	-	11,040.0	0.24	0.00002	0.009	1/4
48(b)	26	20	0.47	0.37	0.08	1.5×10^{-3}	55.0	0.24	0.004	0.008	1/4
50	23	26	0.55	0.62	0.22	5.2×10^{-3}	42.0	1.0	0.024	0.020	1
51	Neg.	12	-	0.20	Neg.	-	60.0	20.0	0.340	0.059	1
52	23*	29	0.54	0.67	-	-	43.0	10.0	0.23	0.043	2
53	Neg.	11	-	0.44	Neg.	-	25.0	20.0	0.79	0.085	2

*Measured from micrograph.

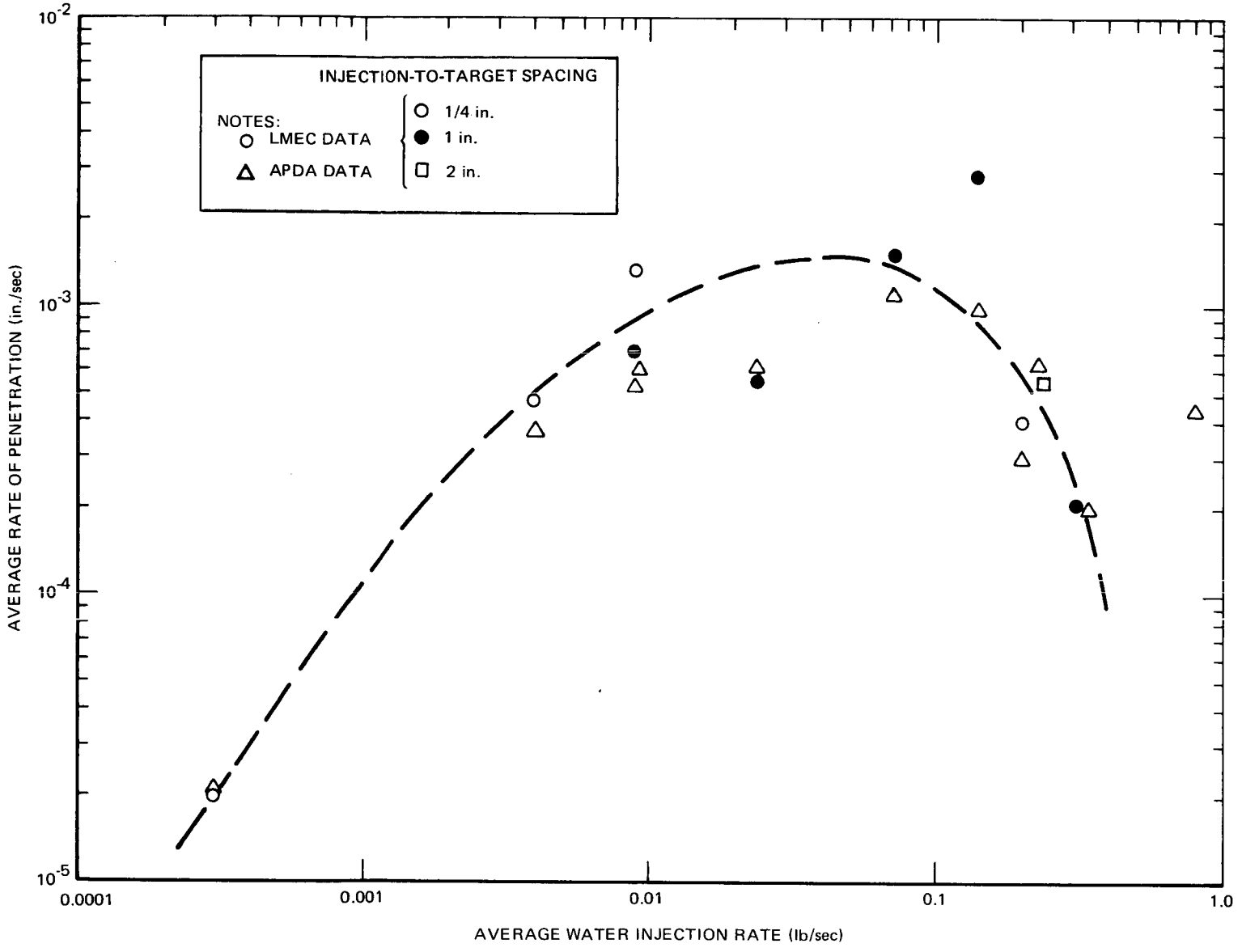

Figure 17. Effect of Water Injection Rate on Primary Target-Tube Wastage Rate

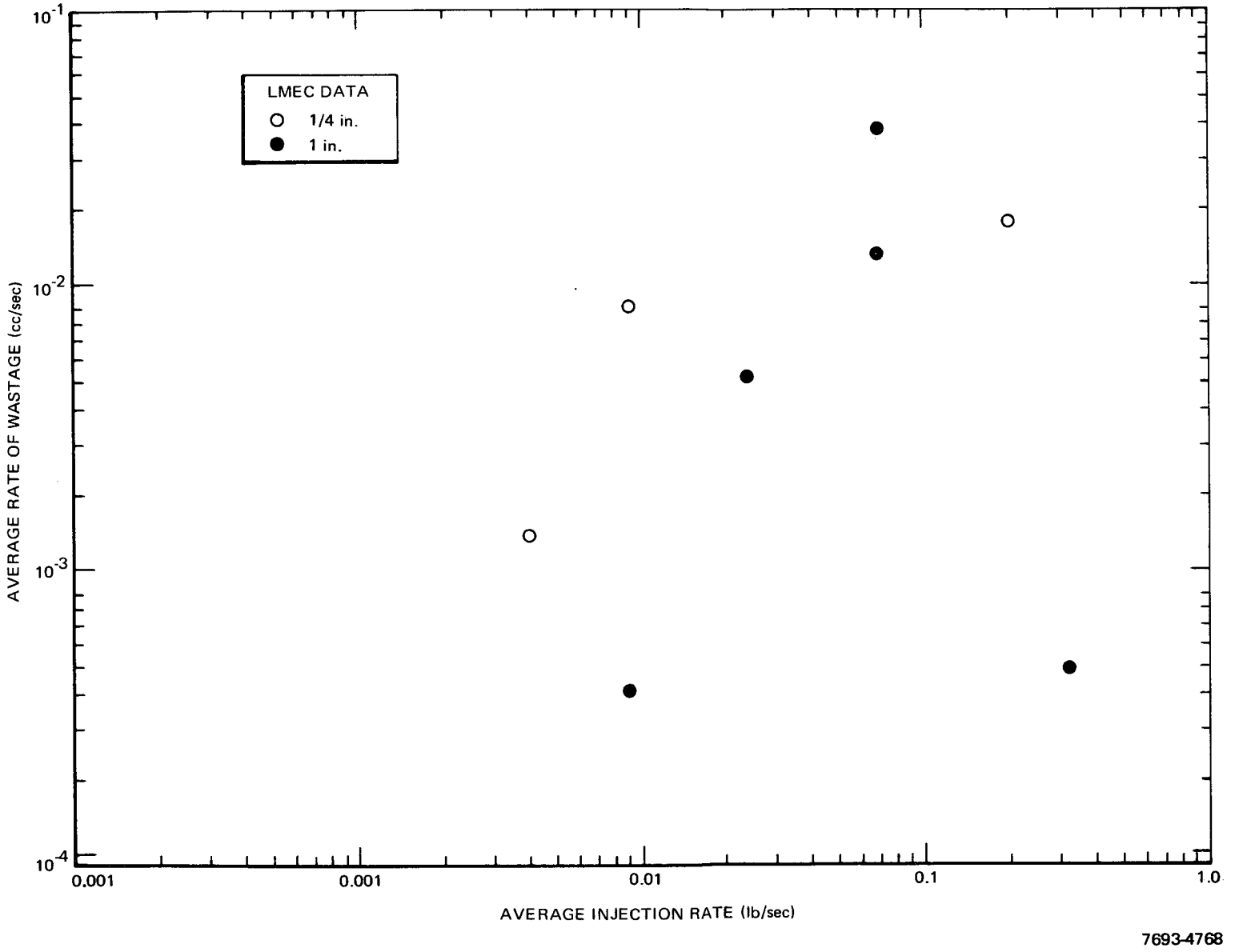

Figure 18. Effect of Water Injection Rate on Volume Wastage Rate

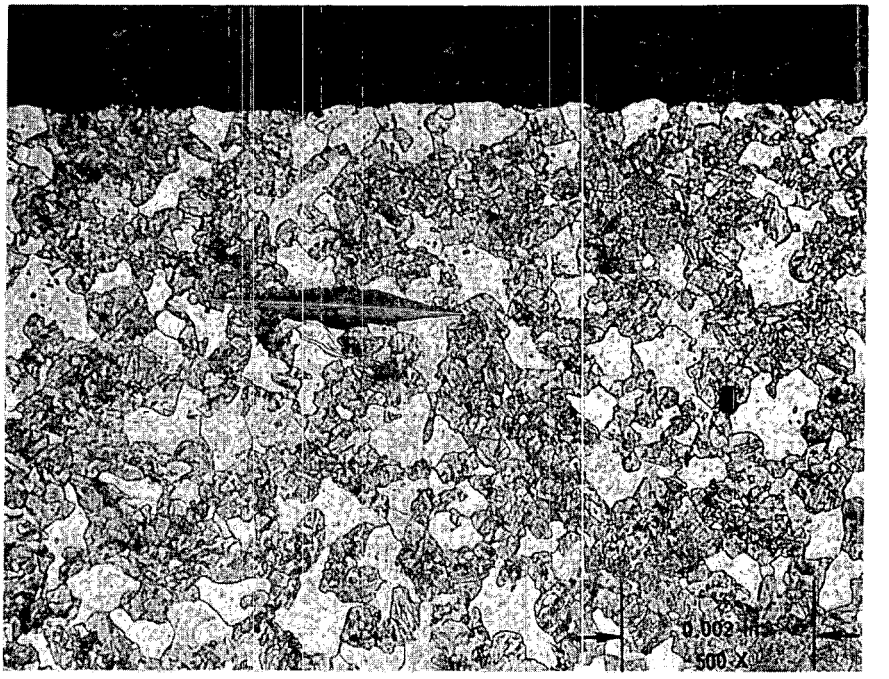

a. Primary Target Tube

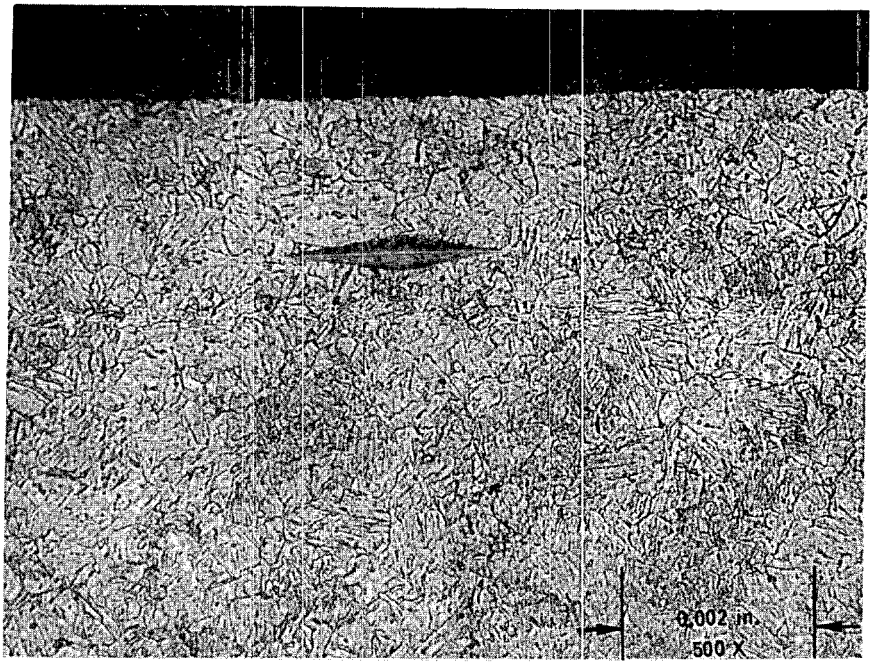

b. Secondary Tube

7693-4769

Figure 19. Typical Micrographs of the Outside Diameter Surfaces in Wastage Areas -- Note the Absence of any Corrosion

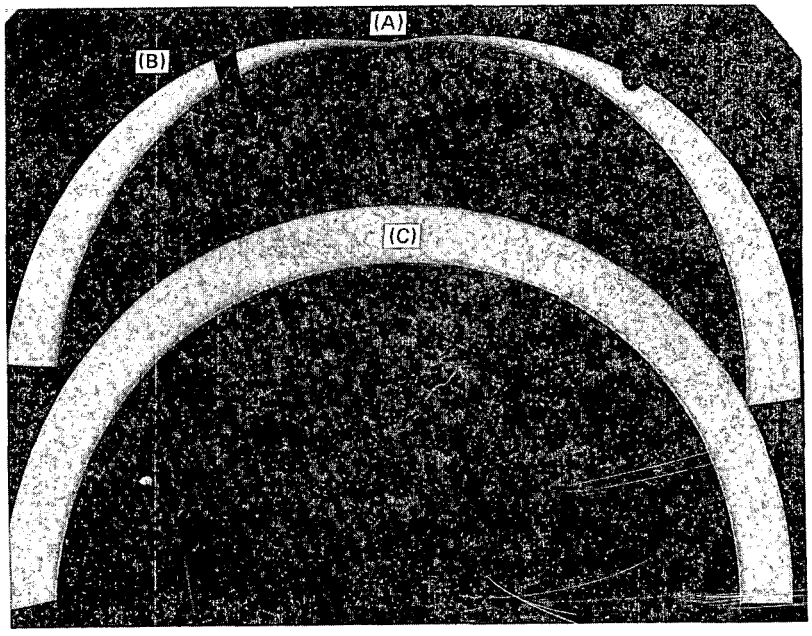

7693-4770

Figure 20. Macrograph of Tube TR47A-2 (Secondary Tube) Showing the Thin Wastage Areas, A and B, and the Areas 180 Degrees Away from the Wastage, C

From the measurement of inside diameter displacement on the figure, the bending deflection is found to be 0.03 in., which is attributed to droplet impact. Further microscopic evidence of mechanical damage due to droplet impingement is supported by scanning electron microscopic work, as shown, for example, in Figures 7 through 9. Therefore, the conclusion that the material removal process was controlled primarily by impingement or erosion is supported by: (1) the presence of droplet craters in the wastage areas; (2) the presence of plastic bending (deflection) in the wastage areas; and (3) the absence of any corrosion in the indented wastage areas. This conclusion is in full agreement with that reported in a previous examination.[3]

From the conditions of the water-injection test in Rig 10, it is not surprising to find that the wastage could be controlled by erosion, as explained in more detail in the next section.

C. EFFECT OF SHOCK LOADING ON MATERIAL

1. Dynamics of Shock-Loading Due to Water Impingement

In the sodium-water reaction tests conducted in APDA's Rig 10, water was forced through a very narrow capillary passage (ranges from 0.008 to 0.128 in.) at a high rate because of the prevailing high-pressure differential between the water injection system and the sodium-water reaction chamber. In a computer model for the impingement effects of a small water leak in a sodium-heated steam generator, Perry and Bomelburg[4] have indicated that, as the water is depressurized, it will flash and the resulting wet steam will be accelerated to high supersonic velocities, thus forming a supersonic jet at the injection tube exit. This supersonic jet essentially consists of water droplets in the core, steam and possibly entrained sodium droplets in the periphery of the jet. If the jet encounters a target tube, a detached shock wave will form closely ahead of that tube.[4] As further postulated by Perry and Bomelburg, the vapor phase of the jet will be decelerated abruptly to lower (subsonic) velocities. However, the liquid phase (water droplets) will essentially retain its velocity, and impact on the obstacle with almost its high, preshock velocity. A relationship correlating the one-dimensional transient impact pressure with velocity of droplet has been derived and is shown as follows:[4]

$$P = \rho_4 \left[(a_4 - 2\, b\alpha)\, U_2 + b\beta \right] \qquad \ldots (1)$$

where

$$\alpha = \frac{a_4 R + c + 2\, du_1}{2\,(bR - d)}$$

$$\beta = \frac{cu_1 + du_1^2}{bR - d}$$

$$R = \frac{\rho_4}{\rho_1}$$

$$U_2 = -\alpha + \sqrt{\alpha^2 + \beta}$$

and

P = transient impact pressure on the steel target

ρ_1, ρ_4 = densities of water and steel, respectively, at 1 atm

a_4 = sound velocity in undisturbed steel

c = sound velocity in undisturbed water

d, b = empirical constants

u_1 = velocity of liquid droplet before impact.

Based on the test conditions reported for APDA's Rig 10 small-leak tests, the above relationship was programmed to compute the transient impact pressure as a function of water droplet velocity. The results are reproduced in Figure 21.[4] For the highest droplet velocity computed by Perry and Bomelburg (3056 fps), the maximum computed transient impact pressure is 4×10^5 psi,* which is somewhat below the Hugoniot elastic limit for iron (~130 kbars or 1.9×10^6 psi). However, these velocities are sufficiently high to cause local damage to the steel, as indicated in a number of test reports.[5,6] In addition, depending on the volume of injected water, the number of droplets available for impingement can be very large. For example, for test 47, the number of water droplets was estimated to be in the order of 10^{17} droplets for 20 lb of injection water. This calculation was based on the average droplet crater size of 1 micron, as measured from scanning electron micrographs. It can be seen, therefore, that this large number of droplets, coupled with their high impact stresses, could produce extensive damage (erosion) due to multiple droplet impact.

Before continuing the discussion of impact pressure due to shock, it will be helpful to review some essential points about the effect of shock-loading on iron or iron alloys.

*Because of the many simplifying assumptions made in computing these pressures, they should be considered only to be correct within an order of magnitude.

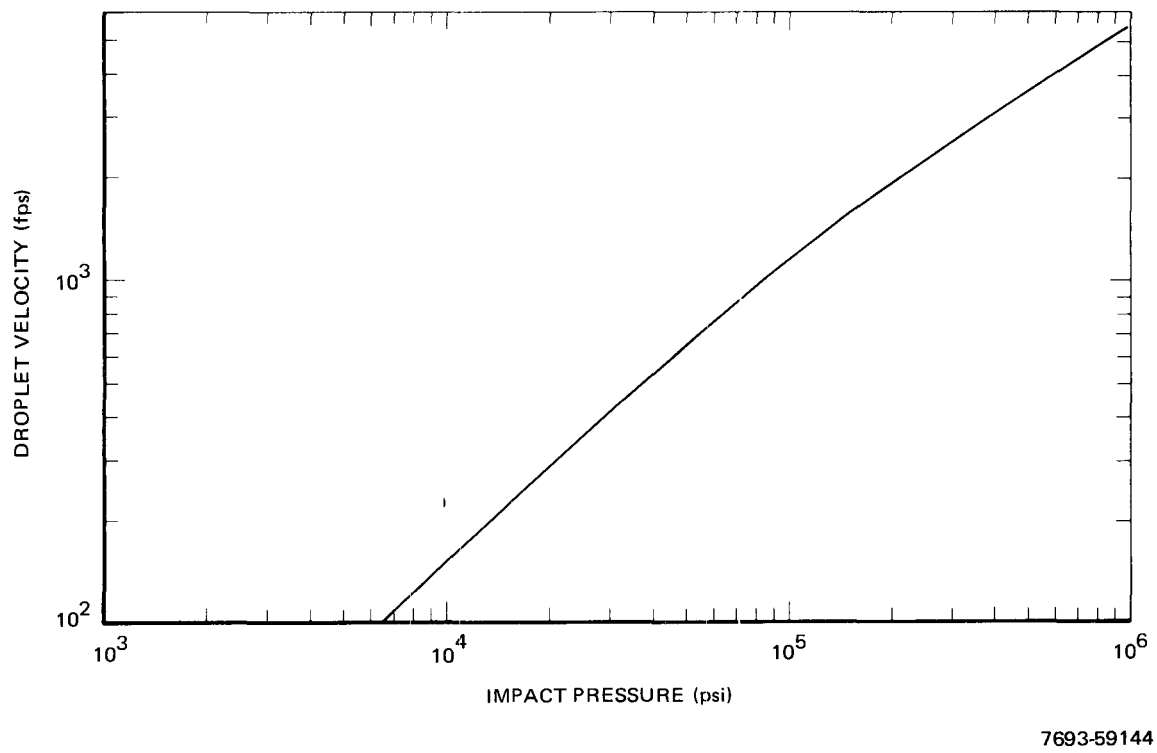

Figure 21. Transient Impact Pressure on a Steel Target as a Function of Water Droplet Velocity[3]

2. Effect of Shock-Loading on Fe and Fe Alloys

a. Hugoniot Curve for Fe and Fe Alloys

A basic description of the behavior of a metal or alloy in shock loading, such as that produced by detonation of an explosive, is given by the equation-of-state curve or Hugoniot curve. The Hugoniot curve for iron is shown in Figure 22, which displays a distinct and well-documented discontinuity at a pressure of 130 kbar ($\sim 1.9 \times 10^6$ psi).[7] The marked change in slope of the curve has been attributed to a pressure-induced polymorphic transformation from body-center-cubic (BCC) α-iron to face center cubic (FCC) γ-iron.[8] Brancroft, Peterson, and Minshall[8] have suggested that this transformation is the normal A_3 transformation in Fe (from BCC to FCC lattice) depressed from 910°C (1670°F) to approximately 37°C ($\sim$98°F) by the high pressure. However, recent data indicate that the temperature coefficient of the critical pressure is much less than predicted by the model.[9] Duff and Minshall[10] reported that the pressure of the transition may also depend on the initial target temperature.

The transition pressure is reported to increase with carbon content and the alloying elements in iron.[11] The effect of Ni or Cr concentration is shown in Figure 23. The equation-of-state data are presented in Figure 24 for various Cr concentrations.[11] The effect of Mo in Fe is not known at the present.

b. Shock Loading Effects on Microstructure

There are many references in the literature which report the results of shock loading of Fe and Fe alloys.[11-14] From a survey of these references, it becomes apparent that Fe and Fe alloys exhibit two major characteristics when loaded impulsively: (1) formation of mechanical twins (Neumann bands) in the ferrite grains, and (2) increase in hardness and strength.

Normally, in iron at low temperatures and/or at high strain rates, twinning takes place before plastic deformation by slip has occurred. For polycrystalline materials, the nonuniformity of stress, coupled with individual grain orientation, results in a fairly wide pressure range for twinning. For shock loading, it appears that the twinning is produced by the elastic I wave.[15] Thin mechanical twins are found in iron alloy even when shocked to as low as 14 kbar ($\sim 2 \times 10^5$ psi).[16] The number of twins increases with increasing pressure. When the pressure exceeds 130 kbars, the microstructural features become much finer. There is no easily discernible difference in the microstructure as the pressure increases from 130 kbars to 350 kbars.[17] The twinning frequency is also influenced by the material conditions (Figure 25), as well as by the angle between the shock direction and specimen surface (Figure 26). Moreover, it is noteworthy that heat treatment has a significant effect on twin markings of commercial steels.[15] After shock loaded from 45 kbars to 75 kbars, twin markings were observed on all steel specimens with 0.25% to 1% C which had been either annealed or spheroidized, but no twins were observed on quenched samples or on samples which had been quenched followed by tempering at lower temperatures.

It is known that the passage of a high-pressure shock wave through a material results in a temperature rise in the material. Temperature estimates for iron, under shock, have been reported and are reproduced in Table 5.[15] As shown, the temperature rise increases with the pressure. As a consequence

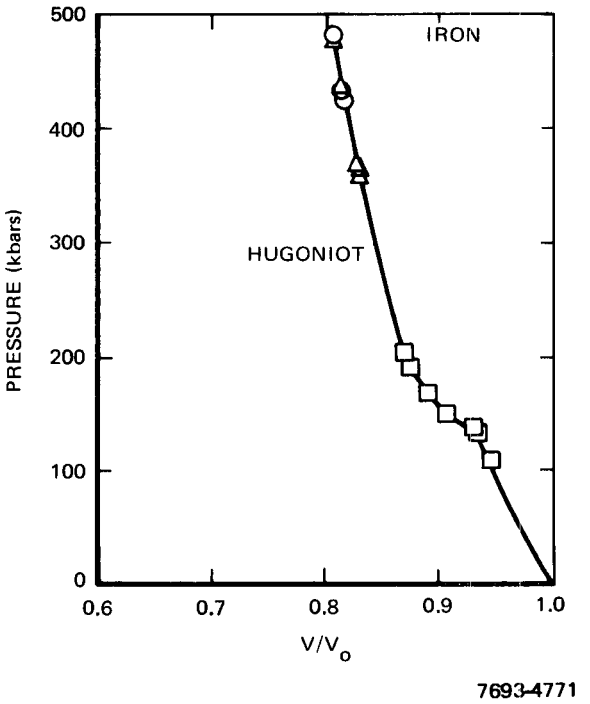

Figure 22. Hugoniot Curve for Iron[7]

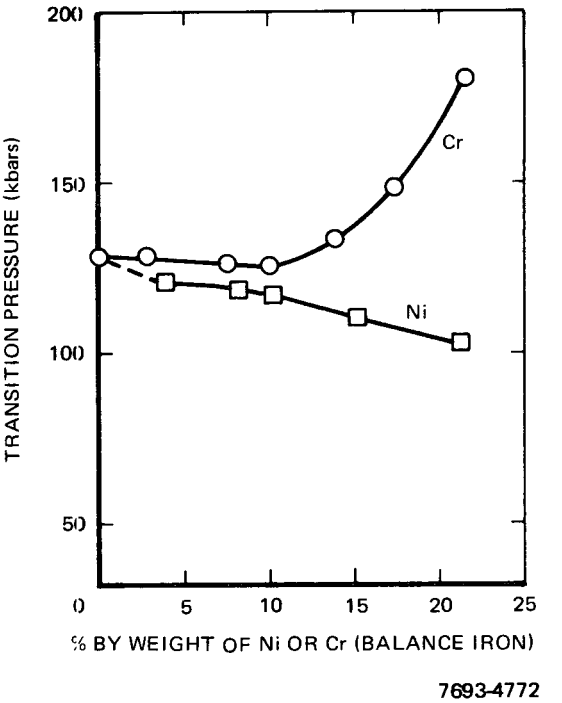

Figure 23. Variations of Transition Pressures with Ni and Cr Content in Iron Alloys[11]

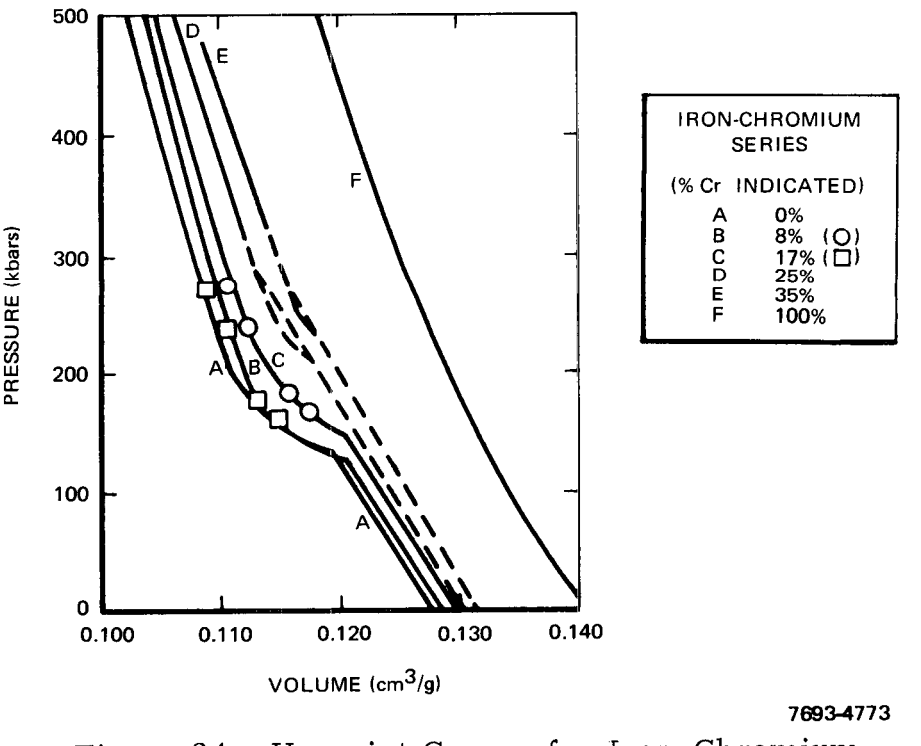

Figure 24. Hugoniot Curves for Iron-Chromium Alloys[11]

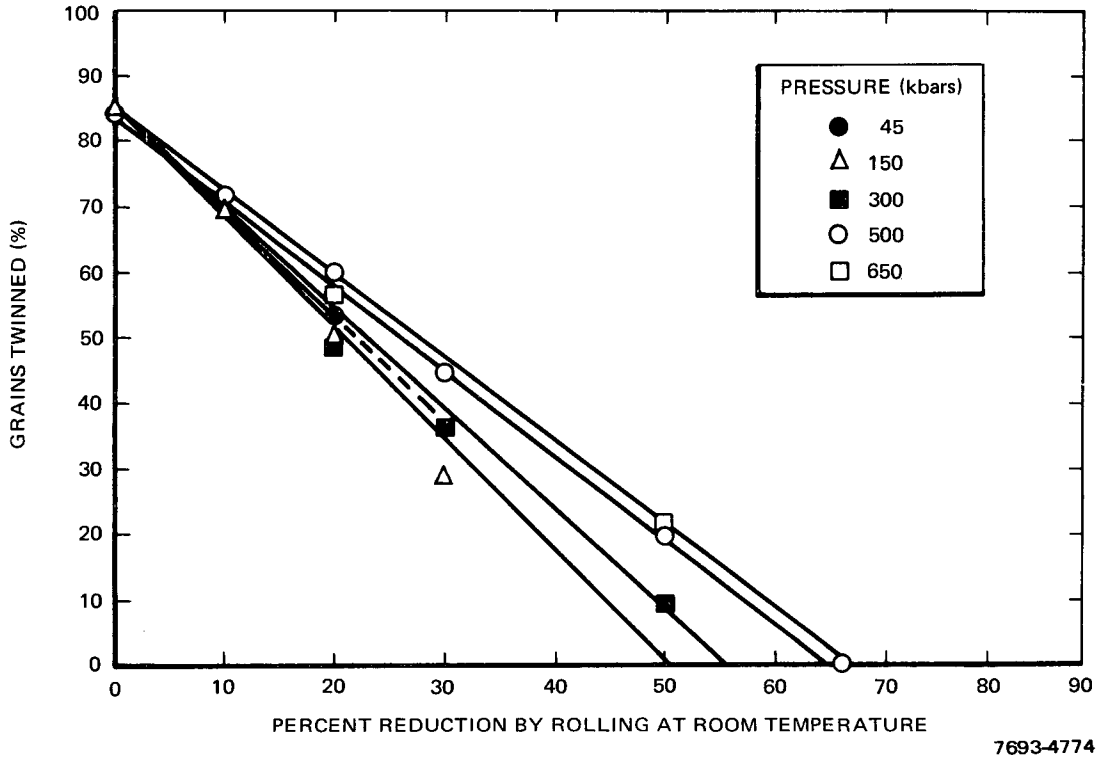

Figure 25. Effect of Cold Rolling on Twinning by Shock Loading(14)

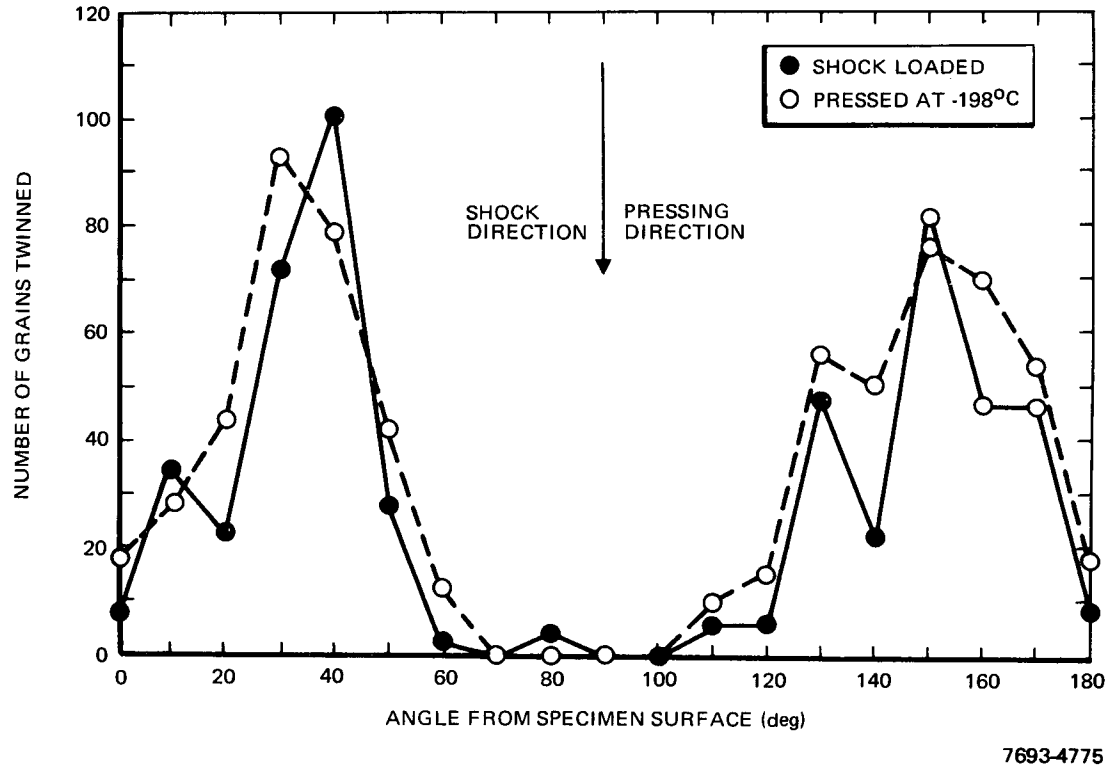

Figure 26. Distribution of Twins Oriented at Various Angles to the Specimen Surface in Iron after Pressing in Liquid Nitrogen and after Shock Loading to 500 kbars(14)

TABLE 5[15]

EFFECT OF SHOCK PRESSURE ON THE CALCULATED TEMPERATURE AT PRESSURE

Shock Pressure (kbars)	Calculated Temperature at Pressure (°C)
130	60
350	350
500	550
750	1050

Note: Based on the assumption of iron shocked at 20°C

of this heating effect, the energy absorbed from a 650-kbar or higher pressure shock is sufficient to cause localized recrystallization. Recrystallization is reported for iron shock-loaded to 750 kbars.[15]

c. Shock Loading Effects on Hardness

As indicated in the previous section, the shock loaded Fe or Fe alloys also display changes in mechanical properties, such as in hardness and strength. The magnitude of change increases with pressure. For pressures below 130 kbars, only a moderate increase in hardness is found with pressure. For pressures above 130 kbars, a rather rapid increase in hardness is found with pressure up to 220 kbars, as shown in Figure 27.[17] The increase in hardness due to shock loading is attributed primarily to:

1) The pressure-induced phase transformation that occurs for Fe and certain other ferrous alloys (for $P > 130$ kbars). Although the details of this phase transformation are still unknown, it is to be expected that the high degree of lattice strain and the complex microstresses developed during the phase change will produce a high hardness.

2) Twins produced by shock loading to pressure below the Hugoniot elastic limit for iron. Twinning can contribute an appreciably greater hardening effect if a large number of fine twins are produced, as in the pressure region close to 130 kbars. Increased twin density (i.e., number of twins and finer twin spacing) will increase hardness.

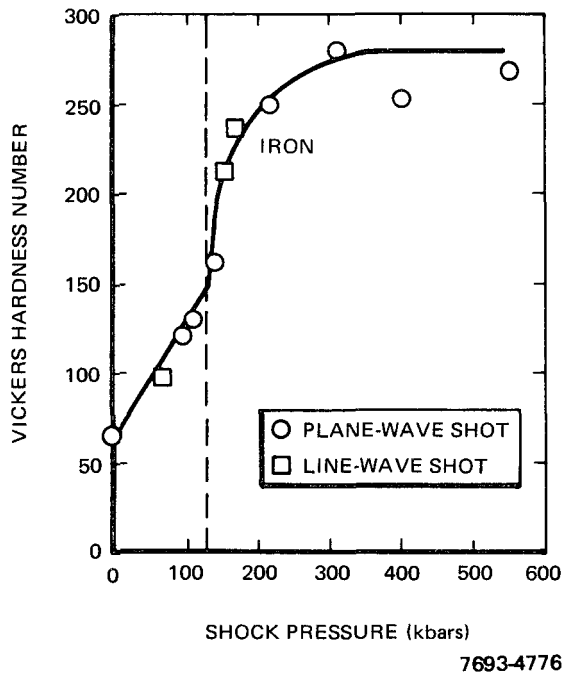

Figure 27. Hardness vs Shock Pressure for Iron[17]

3) Plastic deformation in which slip occurs, as in room temperature deformation of Fe/Fe alloy at slow strain rates. In the case of explosive hardening, because there is only a small percentage of gross deformation and no microscopically visible grain distortion,[15] it is hard to rationalize hardening in terms of slip process. Moreover, theory predicts that fast-moving dislocations are efficient producers of vacancies and interstitials.[18] While it is attractive to speculate on hardening arising from a high concentration of point defects, no experimental evidence is available at present to confirm this hypothesis. On the other hand, it is possible that the instantaneous temperatures produced during shock loading at high pressures are sufficient to anneal out most of the point defects produced by shock loading.

3. Effect of Shock Loading on APDA Target Tubes

In view of the preceding discussion of shock loading effects on Fe or ferrous alloys, it is interesting to note the following observations on the primary target tubes:

1) No twinning bands or Neumann bands were observed in any of the examined target tubes.

2) No microstructural or phase changes were detected.

3) No apparent increase in hardness was noted in the wastage areas.

4) Plastic deformation lines were observed in only some of the surface grains in the wastage areas.

Based on the one-dimensional computer model of droplet impingement,[4] and on the test conditions in APDA's Rig 10, the most severe transient impact pressure estimated is 4×10^5 psi, which is below the Hugoniot elastic limit for Fe ($\sim 1.9 \times 10^6$ psi). Therefore, it is understandable that there was no phase change in the impacted target tube. However, under shock loading of this magnitude, twinning bands or Neumann bands are normally expected to be present in the ferrite grains of 2-1/4 Cr - 1 Mo steel. For instance, Zukas and Fowler[15] observed extensive twinning ($\sim$85% of grains) in annealed iron when shock loaded to 45 kbars ($\sim 6 \times 10^5$ psi). Some twinning was reported in ferrous alloys shocked to pressures as low as 2×10^5 psi.[16] Because of the many simplifying assumptions made in the computation, the transient impact pressures obtained should be considered only to be correct within an order of magnitude. Therefore, the actual transient impact pressure could be below 10^5 psi, which may be too low for twinning to occur. However, in addition to pressure, twinning is also dependent on temperature, grain size, alloy content, and material condition. Figure 28 shows the effect of test temperature on the critical resolved shear stress for twinning and slip in a typical BCC metal.[19] As shown, yielding occurs by twinning when temperature $T < T_t$ (critical twinning temperature) and by slip at $T > T_t$. It is known that T_t is not constant for a given material, but varies with strain rate, grain size, and material conditions (i. e., annealed or cold-worked). It should be noted that the tests in APDA's Rig 10 were conducted at approximately 600°F, which is believed to be too high for twinning to take place in iron. In addition, quenched commercial steel samples, or samples which had been quenched followed by tempering at lower temperatures, are reported to show no twinning after shock loading to 45 and to 750 kbars.[15] But samples which had been either annealed or spheroidized showed twins.[15] Biggs and Pratt[20] reported that decarburization or prestrain at ambient temperature can

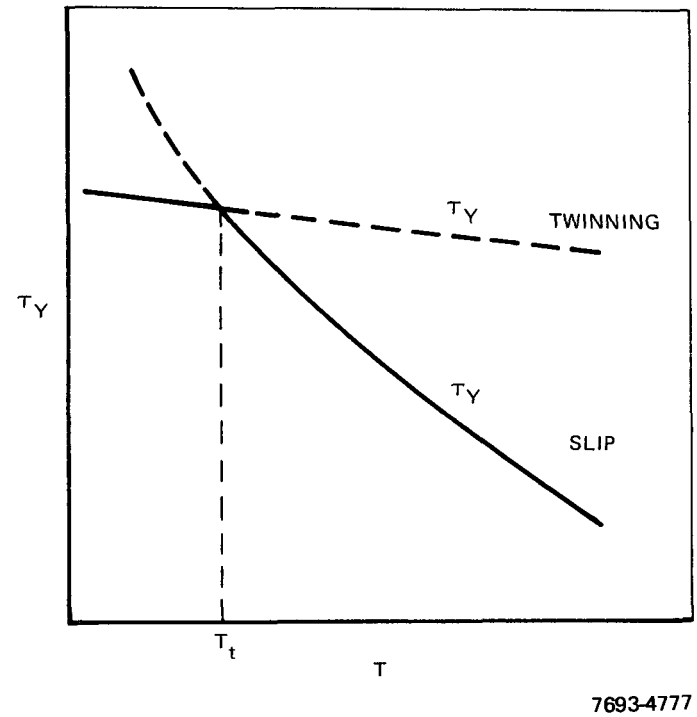

Figure 28. Effect of Test Temperature on the Critical Resolved Shear Stress τ_Y for Slip and Twinning in a Typical BCC Metal. Yielding Occurs by Twinning When $T<T_t$ and by Slip at $T>T_t$ (19)

also prevent twinning. In the target tubes examined, some surface decarburization and minor cold work indications were found; but since the history of the target material is not known, the effects of heat treatment and material condition on twinning of target tubes could not be ascertained.

It can be seen, therefore, that the absence of twinning in the impact areas of the target tube is probably attributed to one or a combination of the following reasons:

1) Thermal treatment or transient in the target tubes, which retards twinning when shock loaded, such as that reported by Zukas and Fowler.(15)

2) The prevailing high temperature conditions, which may be too high for twinning to occur.

3) Conditions of the target material prior to shock loading.

4) The magnitude of shock which could be too low for twinning to take place.

As presented in Table 3, there is no change in hardness in the wastage areas of the primary target tubes when compared to other areas away from wastage. With an estimated shock impact pressure of 4×10^5 psi, the hardness in the steel should, in general, increase for iron (Figure 27). Specifically, at 25 kbars ($\sim 3.6 \times 10^5$ psi) pressure, the hardness of shocked iron is reported to increase about 30%, i.e., from Vicker's Hardness Number (VHN) 65 to VHN 85.[17] However, the insensitivity of hardness to shock loading on the target tubes can possibly be explained by the aforementioned reasons suggested for the lack of change in microstructure.

In summary, the transient shock impact pressure produced by water injection did not affect the microstructure and hardness of the material in the wastage areas, in consonance with the previously published sodium-water reaction data.[3]

D. EFFECT OF TEMPERATURE RISE

1. Wastage of Secondary Tubes

As noted in the previous section, the primary target tubes did not exhibit any apparent microstructural (i.e., twinning, phase change, or recrystallization) or hardness changes. However, for all the secondary (or adjacent) tubes examined, significant changes were found both in microstructure and in hardness, as shown in Figure 4 and in Table 3, respectively. Specifically, for tube 47-A2, the microstructure in the wastage areas exhibited a coarse bainite structure with virtually no proeutectoid ferrite grains (Figure 4). In areas 180 deg away, however, the microstructures displayed a normal bainite structure with large, proeutectoid ferrite grains (Figure 5). This microstructural change is attributed to thermal excursion due to the exothermic sodium-water reaction and subsequent quenching by flowing sodium at a much lower temperature ($\sim$600°F). Based on comparison with controlled microstructures produced by quenching 2-1/4 Cr - 1 Mo steel,[3] the maximum temperature could have reached 1800°F in the wastage area of the secondary tube. But for the primary target tube, the maximum temperature estimated is only 1400°F; the most probable temperature reached could have been much lower ($\sim$1200°F). From the Time-Temperature-Transformation Curve for 2-1/4 Cr - 1 Mo steel (Figure 29), the microstructure produced by quenching from 1700 or 1800°F to 600°F should consist of only bainite without the presence of proeutectoid ferrite,[21] in agreement with the microstructures observed in the wastage areas.

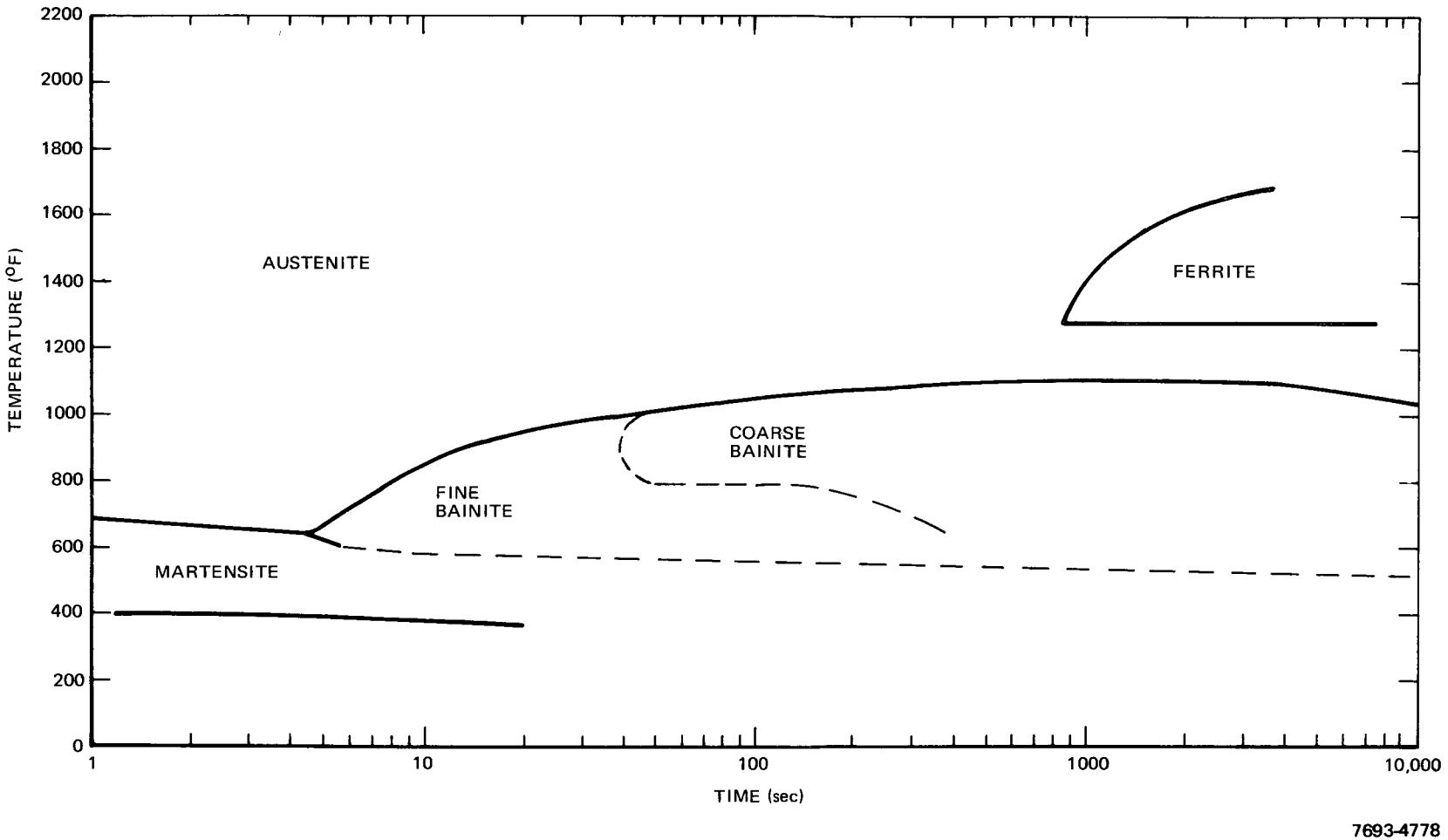

Figure 29. Continuous-Cooling Transformation Diagram for 2-1/4 Cr - 1 Mo Steel[21]

Hardness comparison between the wastage areas and areas 180 deg away from wastage also disclose a significant hardness increase. Specifically, for tube 47-A2, the average hardness in the wastage area is 391 KHN, and the average hardness in areas 180 deg away from wastage is only 228 KHN. Again, these hardness data indicate that the material in the wastage area could have experienced a high temperature ($\gtrsim$1800°F) and then a rapid quench to bulk sodium temperature ($\sim$600°F), in consonance with the microstructural observations. Similar changes in microstructure and in hardness were found for all other examined secondary tubes. Hardness increase in the wastage areas for tube TR46-B3 is 211 KHN (i.e., 394 KHN vs 183 KHN); for tube 47-A3 it is 119 KHN (i.e., 313 vs 194 KHN). Tube 46-A-2 did not exhibit any change because there was no measurable wastage (Table 2).

2. Effect of Tube Location on Wastage

As additionally noted in the preceding section, there are significant differences in wastage, in microstructure, and in hardness between the primary and secondary (adjacent) impacted tubes. These observations suggest that the path length between the injection orifice and the tube may play a significant role in wastage. The critical location of the tube is defined as the location where the majority of the jet of water droplets would be moderated to sufficient low velocities for sodium-water reaction to occur. To illustrate this point, consider test 47 in which two secondary tubes were completely penetrated by wastage. The location of the injection orifice relative to the primary target tube and to the secondary tubes is shown in Figure 1. While the path length between the injection orifice and the primary target tube is only 1 in., the distance between the injection point and any secondary tube in Row A (Figure 1) is at least 3 in., depending on the tube of interest. The primary target tube (tube 47-C4) exhibited a penetration depth of only 0.013 in., the walls of two secondary tubes in Row A (tubes 47-A2 and 47-A3, 0.065 in. nominal wall thickness) were completely penetrated: a five times increase in penetration depth relative to that of the primary target tube. In addition, the measured volume of wastage for the primary target tube is 0.03 cc; for secondary tubes 47-A2 and 47-A3, wastage volumes are 1.62 and 1.45 cc, respectively. The volume of wastage for the secondary tube is, therefore, more than 50 times that exhibited by the primary target tube. Hence, if other test parameters (e.g., water purity, pressure, temperature, initial jet

velocity, orifice size, angle of deflection, volume of water, etc.) are kept constant, the wastage appears to increase with path length from the injection point in a complex manner, contrary to the behavior of droplet velocity which eventually decreases with distance from the point of injection.[4] It is postulated that this increased path length contributes to increased wastage through a combination of the following effects:

1) Agitation and mixing of reactants, promoting sodium-water reaction;
2) Increased time available for sodium-water reaction initiation; and
3) Reduced velocity of the reactive stream, permitting more water droplets to participate in the reaction.

The preceding observed differences between the primary target tube and the secondary tubes suggest that, in addition to high impact pressure and large number of droplets obtainable under the test conditions in Rig 10, a prevailing high-temperature condition on the tube impact region is also necessary for the extensive wastage observed in some of the secondary tubes. It is surmised that the heat of reaction of sodium and water or steam (or both) could have provided the required thermal energy for the temperature increase. Therefore, the magnitude of wastage on the tube appears to depend on: (1) the probability of a "massive" sodium-water or steam reaction on or near that tube; (2) the volume or number of droplets or particles that participated in the massive sodium-water reaction and impingement processes; and (3) the velocity (therefore, the impact pressure) of the deflected droplets or particles that impinged on the tube.

From the observed wastage data on the tube bundle, it is apparent that the probability of a massive sodium-water reaction to occur on or near a secondary tube depends on: (1) the distance of the tube from the injection orifice; (2) the path of the deflected jet of water droplets and steam particles; (3) the extent of mixing between sodium and water or steam; and (4) the mean velocity of the jet or stream of water droplets. The volume and velocity of deflected water droplets or steam particles are functions of the original volume of water, the test conditions, the angle of deflection, and path length of the deflected jet or steam.

At this point of discussion, a hypothesis involving a "critical" velocity concept may be introduced to explain the wastage observed in numerous secondary

tubes. It appears that when the majority of the droplet velocities are above a critical velocity (V_c), no major sodium-water reaction can occur because the sodium would just be pushed aside due to high kinetic energy of the jet or steam of droplets or particles. In addition, the jet of droplets would be shielded from sodium by the gas pocket produced by the sodium-water or steam reaction on the periphery of the jet. But when the majority of the droplet velocities are equal to or below V_c, a relatively large-scale sodium-water reaction would occur, resulting in a sudden and drastic increase of temperature at the reaction location. If there is a secondary tube at or near the reaction, extensive wastage (damage) would occur on the tube if there is a sufficient quantity of water droplets or steam particles available for impingement on the tube. Schematic diagrams showing the hypothesized variation of temperature and mean velocity of the jet or stream of droplets on the path length traveled by the stream are shown in Figures 30 and 31, respectively.

3. Effect of Temperature on Erosion Resistance of 2-1/4 Cr - 1 Mo Steel

It is known that erosion resistance usually increases with increased tensile strength and hardness of the material.[22] Any treatment or parameter that will cause an increase of tensile strength or microhardness will, in general, increase erosion resistance. Conversely, any treatment causing any reduction of microhardness or tensile strength will lead to a decrease of erosion resistance. The weakening effect of temperature on tensile strength of 2-1/4 Cr - 1 Mo ferritic steel and on hot microhardness of a ferritic steel is shown in Figures 32 and 33, respectively. In addition, recent impingement damage data on various materials in liquid metals indicate that the severity of impingement damage may be inversely related to the strain energy of the material.[23] Under constant strain rate, the strain energy is defined as the area beneath the stress-strain curve of a material and can be approximated by the equation:

$$E_{(strain)_T} = \left(\frac{\sigma_y + \sigma_u}{2}\right)_T \epsilon_T$$

where

σ_y = yield strength of the material at temperature T

σ_u = tensile strength of the material at temperature T

ϵ_T = elongation of the material at temperature T.

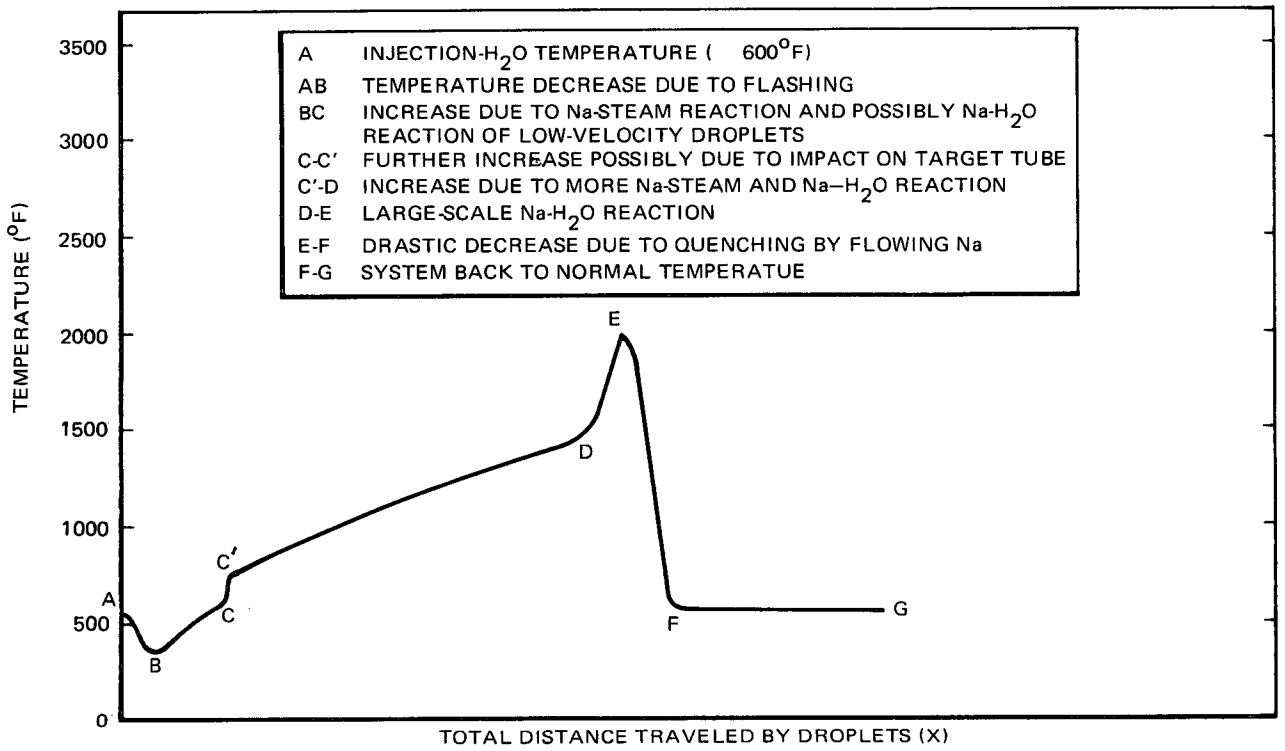

Figure 30. Hypothetical Variation of Temperature with Distance Traveled by Droplet/Jet

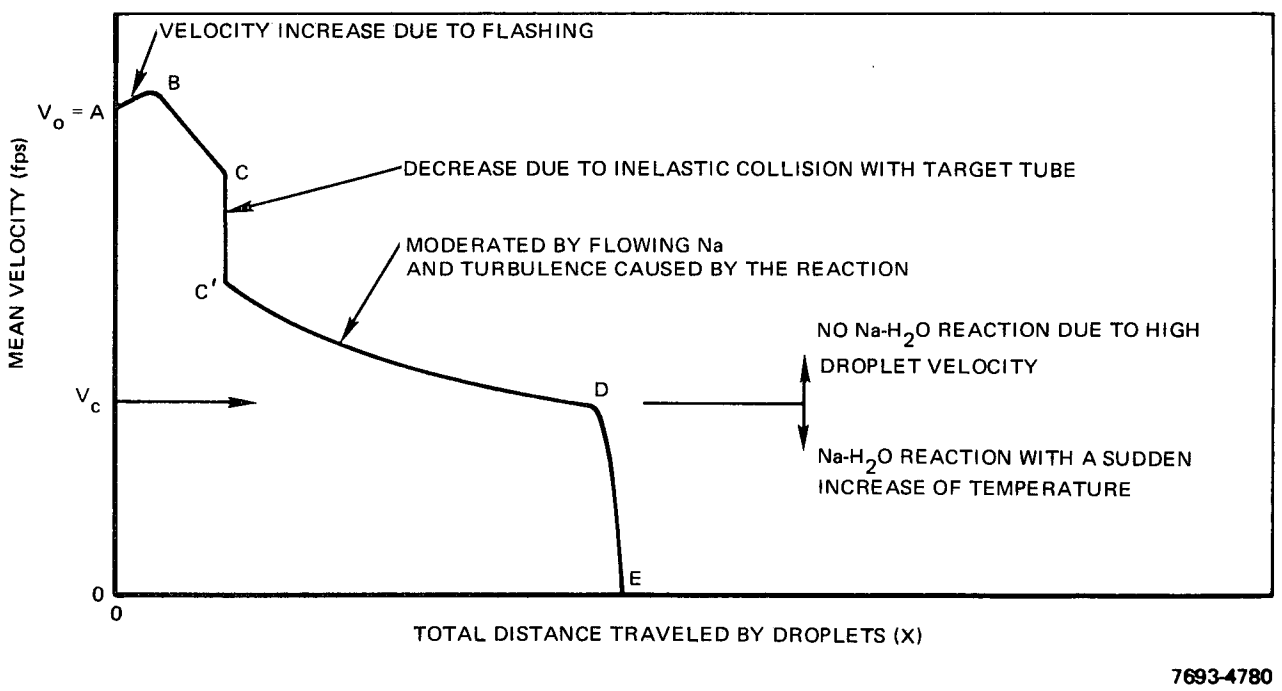

Figure 31. Hypothetical Variation of Mean Velocity of Jet of Droplets with Distance Traveled

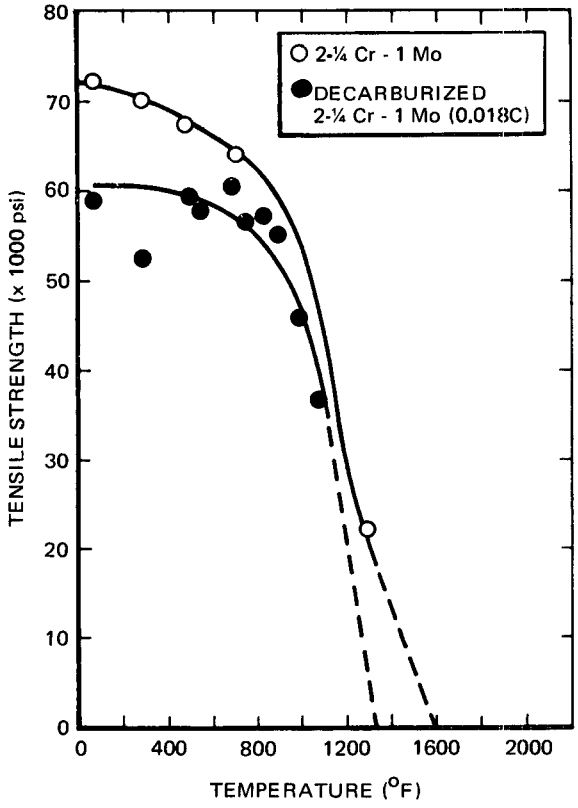

Figure 32. Effect of Temperature on Tensile Strength of 2-1/4 Cr - 1 Mo Ferritic Steel[3]

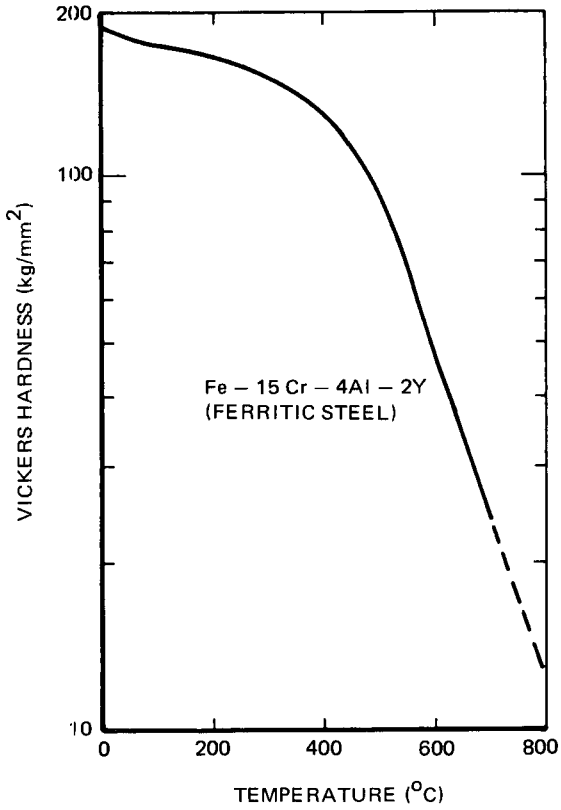

Figure 33. Hot Microhardness Data for a Ferritic Steel[3]

The strain energy of 2-1/4 Cr - 1 Mo steel is reported to decrease with temperature, particularly at temperatures above 1200°F, as shown in Figure 34.

The adverse effect of temperature on ultimate resilience of 2-1/4 Cr - 1 Mo ferritic steel is shown in Figure 35.[3] Ultimate resilience is often a good indication of the resistance of a material to erosion by cavitation.[22]

As previously mentioned in this section, the maximum temperatures reached in the primary and secondary tubes were estimated to be 1400° and 1800°F, respectively. And as reported for test 47, the secondary tubes were found to exhibit a much higher wastage relative to that of the primary target tube. This increased wastage in the secondary tube is attributed to the increase in temperature on the secondary tubes, particularly at temperatures above 1500°F where the strength of 2-1/4 Cr - 1 Mo ferritic steel is almost zero (Figure 32).

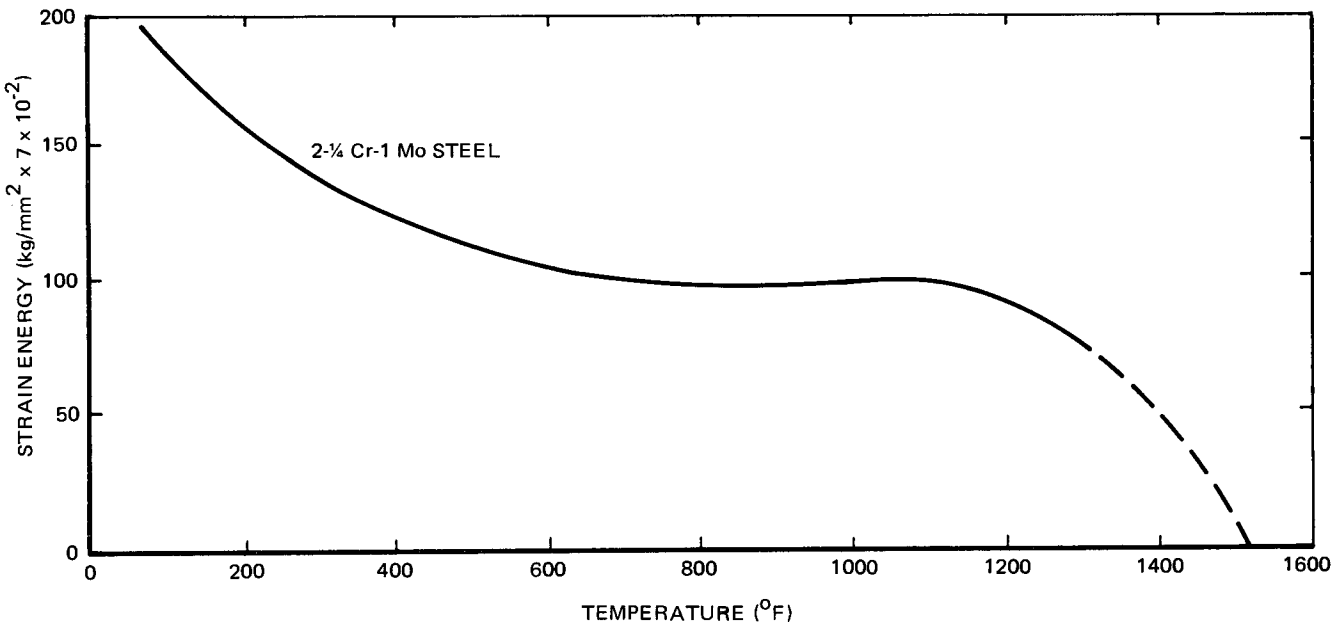

7693-4783

Figure 34. Variation of Calculated Strain Energy with Temperature for 2-1/4 Cr - 1 Mo Ferritic Steel(3)

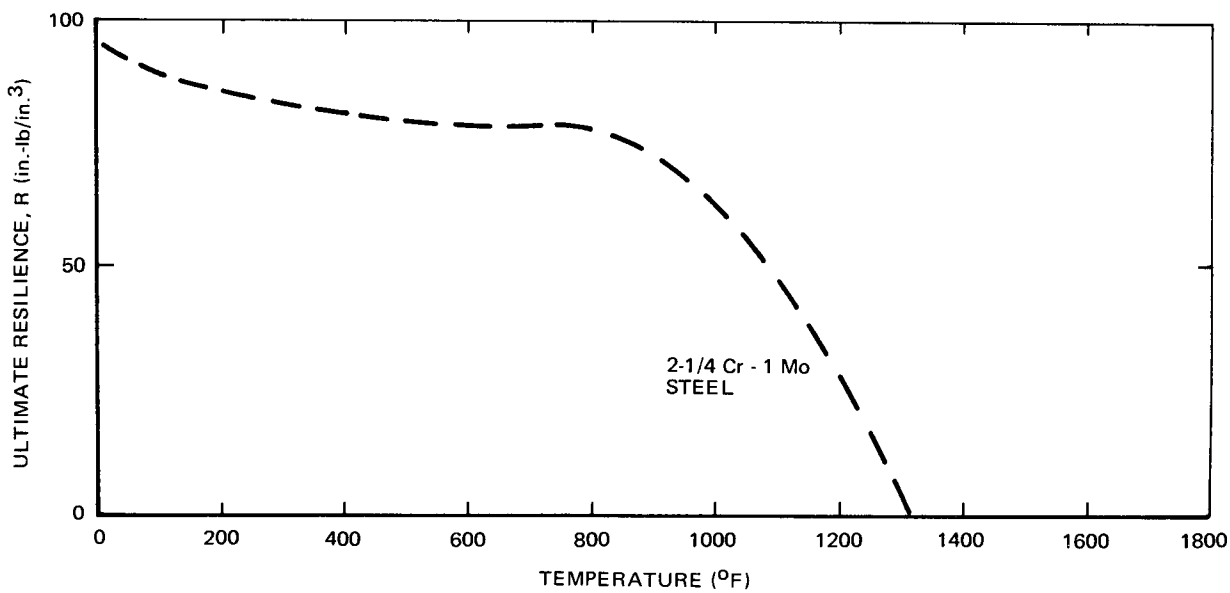

7693-4784

Figure 35. Variation of Ultimate Resilience with Temperature for 2-1/4 Cr - 1 Mo Ferritic Steel(3)

E. MECHANISM OF WASTAGE

In an earlier sodium-water reaction target-tube examination report,[3] the author proposed a wastage mechanism to explain the sodium-water reaction wastage process. As discussed in the report, the wastage process appears to be analogous to a high quality thermal-arc plasma-cutting/hole-piercing process in which the plasma arc rapidly erodes the material, forming a hole/indentation about equal to the diameter of the plasma-arc stream. In the sodium-water reaction tests, the stream would contain a jet of wet steam and/or sodium-water reaction products, traveling at high supersonic velocity, which would impinge on the target material. Material removal would then be controlled by the temperature of the target tube, flow velocity, and the mass of the water droplets in the jet. Material loss (wastage) is attributed to an erosion process resulting from droplet impingement.

Since the completion of examination of 52 more target tubes, additional evidence has been discovered to substantiate the aforementioned wastage mechanism, as well as to refine the proposed wastage mechanism to cover the wastage of adjacent/secondary tubes in the tube bundle. As discussed in previous sections of this report, metallographic, and scanning electron microscopic data on wastage areas have completely established that the material loss (wastage) is attributed to an erosion process resulting from droplet impingement. A recent, and more rigorous, analytical treatment of the impingement effects of a small water leak in a sodium-heated steam generator has shown that a jet of water droplets can be accelerated to very high supersonic velocities (in the order of several thousand feet per second).[4] Because of such high impact velocities, correspondingly high transient impact pressures (10^5 to 10^6 psi) can be generated locally in the impact area of the target tube.[4]

Based on the experimental and analytical data, a more refined wastage mechanism is suggested as follows (shown schematically in Figure 36).

Because of the prevailing high-pressure differential between the water injection system and the sodium-water reaction chamber, the subcooled water is forced through the small diameter injection capillary tube at a high rate. Due to depressurization and subsequent flashing, the resulting jet of wet steam will be accelerated to high supersonic velocities.[4] As schematically shown in Figure 36, the hypothetical steam jet contains, essentially, a core of water droplets

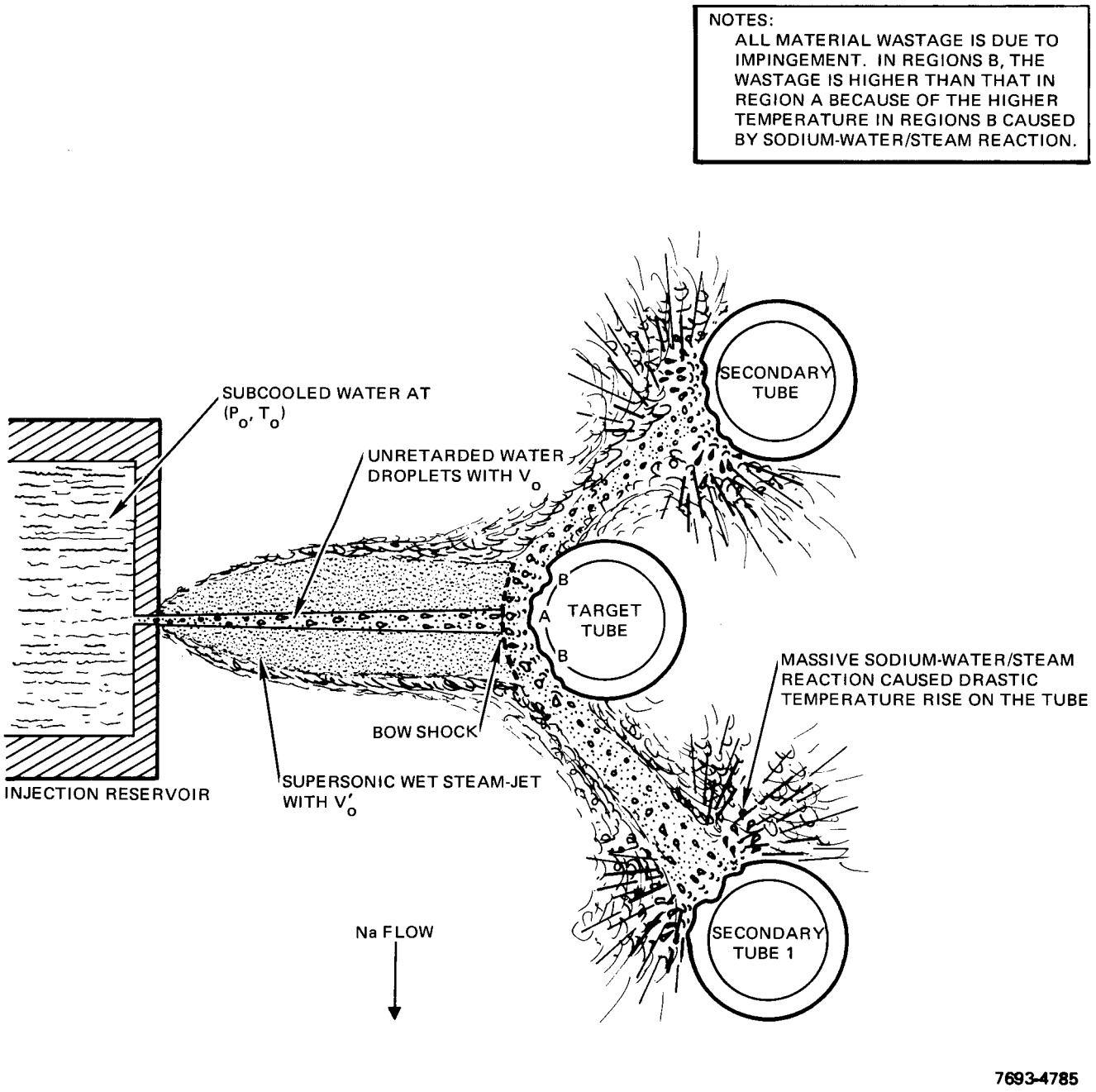

Figure 36. Idealized Configuration of the Droplet Impingement and Sodium-Water Reaction Processes in Rig 10

and a layer of steam and entrained sodium droplets on the periphery. Upon impact on the target tube, the water droplets in the core of the jet will be deflected or scattered inelastically and will continue to traverse with lower velocities. Because of their high velocities, the jet of water droplets will just push the sodium aside and will not result in a major reaction with the surrounding sodium. At this point, the damage produced on the primary target tube can be classified into two main regions, A and B, as shown in Figure 36. Damage in both regions is produced by droplets impingement. Because of sodium-steam reactions in region B, wastage in region B will be higher than in region A because the temperature in region B will be higher than that in region A, resulting in a toroidal pattern of wastage. A typical example of a toroidal pattern at impact is shown in Figure 14.

After deflection from the primary target tube, the jet of water droplets will continue to travel through the sodium without any major sodium-water reaction until most of the droplet velocities have been moderated to or below the threshold velocity V_c. A major sodium-water and/or sodium-steam reaction will follow, resulting in a massive sodium-water reaction and a concomittant drastic increase in local temperature. Hence, the extent of damage (wastage) of the adjacent tubes would depend on: (1) the distance of the tube from the point of massive sodium-water reaction; (2) the volume of the deflected water jet; and (3) the orientation of the tube relative to the deflected jet of water droplets. The hypothetical variations of temperature and velocity with distance are shown schematically in Figures 30 and 31, respectively.

With the test conditions reported for Rig 10, it should be emphasized that the occurence of a major sodium-water reaction, with its instantaneous temperature rise in the impact area, is a necessary requirement for such extensive wastage observed in some of the tubes. As shown by the wastage data for primary target tubes and the secondary tubes, without the drastic temperature rise to seriously deteriorate the strength of the steel, the available transient impact pressure and available number of droplets alone are insufficient to produce such a high wastage.

V. CONCLUSIONS

Based on the dimensional, metallographic, hardness and scanning electron microscopic data obtained from 52 APDA small-leak sodium-water reaction target tubes, it has been found that:

1) Wastage (material loss) resulted primarily from water-jet droplet or particle impingement (or erosion) on the primary target tubes, as well as on the secondary (adjacent) tubes. No evidence of corrosion was found in the impact areas. Droplet impingement craters and permanent plastic straining (bending) were observed in the wastage areas.

2) Under the test conditions in Rig 10, the water injection rate in the range of 10^{-2} to 10^{-1} lb/sec imparted the maximum damage (penetration) rate on the primary target tubes.

3) Tube surface temperature rise caused by sodium-water reaction enhanced the wastage process significantly in all the tubes. For the primary target tubes, a maximum temperature of 1400°F (±100) was estimated. For some of the secondary (adjacent) tubes which exhibited measurable wastage, the estimated maximum temperature is 1800°F (±100).

4) For the secondary tubes, significant hardening and microstructural changes were found in the wastage areas relative to areas 180 deg away from wastage. These changes are attributed to a severe temperature transient experienced by the material in the wastage areas, probably a result of a large-scale sodium-water reaction.

5) For the primary target tubes, no apparent changes in microstructure and hardness were noted in the wastage areas relative to areas 180 deg away from wastage. The lack of change in hardness and in microstructure is probably the result of a small temperature rise in the wastage areas caused by a small-scale sodium-steam reaction.

6) Under the test conditions in Rig 10, the transient impact shock pressure generated by water droplet impact did not affect the microstructure and the hardness of the material in the wastage areas of the

primary target tubes. No twinning bands or Neumann bands were found in the wastage areas.

7) Under certain test conditions, the wastage of secondary (adjacent) tubes can be significantly higher than that of the primary target tube. Specifically, for test 47, the volume wastage of a secondary tube was about 50 times higher than that of the primary target tube. This increase in wastage of secondary tubes relative to that of the target tube is attributed to the drastic increase of temperature on the secondary tube caused by a large-scale sodium-water reaction.

8) Wastage data developed for the secondary tubes strongly indicate that the wastage of a secondary tube is dependent on:

   a) Whether a large-scale sodium-water reaction has occurred on or near the tube; and

   b) The volume of deflected droplets or particles that participated in the final sodium-water reaction and impingement processes.

REFERENCES

1. H. V. Chamberlain et al., "Studies of Material Wastage Resulting from Reaction of Water in Sodium," APDA-254 (June 1970)

2. Facsimile Measure-Image, (Flexbar Machine Corp. Instruction Pamphlet)

3. W. T. Lee, "Examination of Four Sodium-Water Reaction Target Tubes," LMEC-Memo-70-5 (June 26, 1970)

4. R. W. Perry and H. J. Bomelburg, "A One-Dimensional Computer Model for the Impingement Effects of a Small Water Leak in a Sodium-Heated Steam Generator," LMEC-Memo-70-14 (September 30, 1970)

5. N. L. Hancox and J. H. Brunton, "The Erosion of Solids by the Repeated Impact of Liquid Drops," Phil. Trans. Roy. Soc. (London) A260, 121-139 (1966)

6. G. P. Thomas, "The Initial Stages of Deformation in Metals Subjected to Repeated Liquid Impact," Phil Trans. Roy. Soc. (London) A260, 140-143 (1966)

7. J. M. Walsh, M. H. Rice, R. G. McQueen, and F. L. Yarger, "Shock-Wave Compressions of 27 Metals, Equation of State of Metals," Phys. Rev., 108, 196 (1957)

8. D. E. Bancroft, E. L. Peterson, and S. Minshall, "Polymorphism of Iron at High Pressure," J. Applied Phys. 27, 291 (1956)

9. D. E. Curran and P. S. DeCarli, "The Nature of the Phase Transition of Iron at 130 kbars," Stanford Research Institute, Menlo Park, California (1958)

10. R. E. Duff and F. S. Minshall, "Investigation of a Shock-Induced Transition in Bismuth," Phys. Rev. 108, 1207 (1957)

11. F. S. Minshall, "The Dynamic Response of Iron and Iron Alloys to Shock Waves," Proceedings of the AIME on the Response of Metals to High Velocity Deformation, Edited by P. G. Shewman and V. F. Zockay (July 1960), Vol 9, p 299

12. C. M. Fowler, F. S. Minshall, and E. G. Zukas, "A Metallurgical Method for Simplifying the Determination of Hugoniot Curves for Fe-Alloys in the Two-Wave Region," AIME Proceedings on the Response of Metals to High Velocity Deformation, Edited by G. G. Shewman and V. F. Zackay (July 1960) Vol 9, p 275

13. C. S. Smith, "Metallographic Studies of Metals after Explosive Shock," Trans. of AIME, p 574 (October 1958)

14. B. G. Koepke, R. P. Jewett, and W. T. Chandler, "An Investigation of Shock-Hardened Steels by Electron Microscopy," Trans. of ASM 58, 510 (1965)

15. E. G. Zukas and C. M. Fowler, "The Behavior of Iron and Steel Under Impulsive Loading," Proceedings of AIME on the Response of Metals to High Velocity Deformation, (July 1960), Vol 9, p 343

16. J. L. Walters, T. R. Wilshaw, and A. S. Tetelman, "The Effect of Shock Hardening on the Impact Resistance of Low C-Steel," Metallurgical Trans. 1, No. 10, 2849 (October 1970)

17. G. E. Dieter, "Metallurgical Effects of High-Intensity Shock Waves in Metals," Proceedings of AIME on the Response of Metals to High Velocity Deformation (July 1960), Vol 9, p 409

18. J. Weertman, "High Velocity Dislocations," Proceedings of AIME on the Response of Metals to High Velocity Deformation (July 1960), Vol 9, p 205

19. A. S. Tetelman and A. J. McEvily, Jr., Fracture of Structural Materials, (John Wiley & Sons, Inc., New York, 1967), p 158

20. W. D. Biggs and P. L. Pratt, "The Deformation and Fracture of Alpha Iron at Low Temperatures," Acta Met., 6, 694 (1958)

21. R. M. Brown, R. A. Rege, and C. E. Spaeder, Jr., "The Properties of Normalized and Tempered, and of Quenched and Tempered 6-1/4-in.-Thick Plates of 2-1/4 Cr - 1 Mo Steel," ASTM-ASME Symposium on Heat-Treated Steels for High Temperature Service (1966)

22. J. M. Hobbs, "Experience with a 20-KC Cavitation Erosion Test," Symposium on Erosion by Cavitation or Impingement, ASTM-STP 408 (1966)

23. S. G. Young and J. R. Johnson, "Accelerated Cavitation Damage of Steels and Superalloys in Sodium and Mercury," Symposium on Erosion by Cavitation or Impingement, ASTM-STP-408 (1966)

APPENDIX

MACROGRAPHS OF WASTAGE AREAS OF TUBES

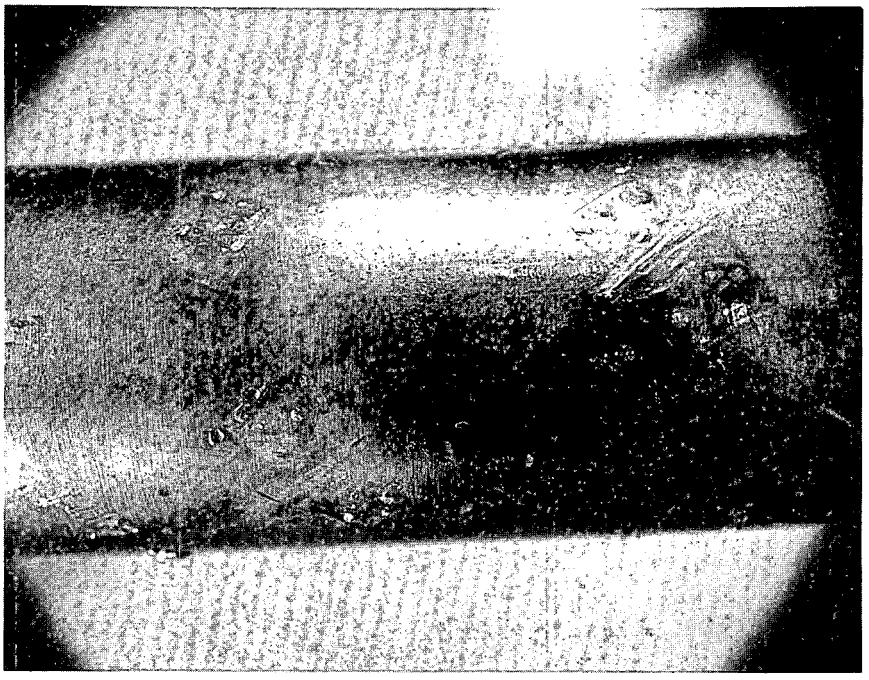

(Mag 2X)

a. Tube 40

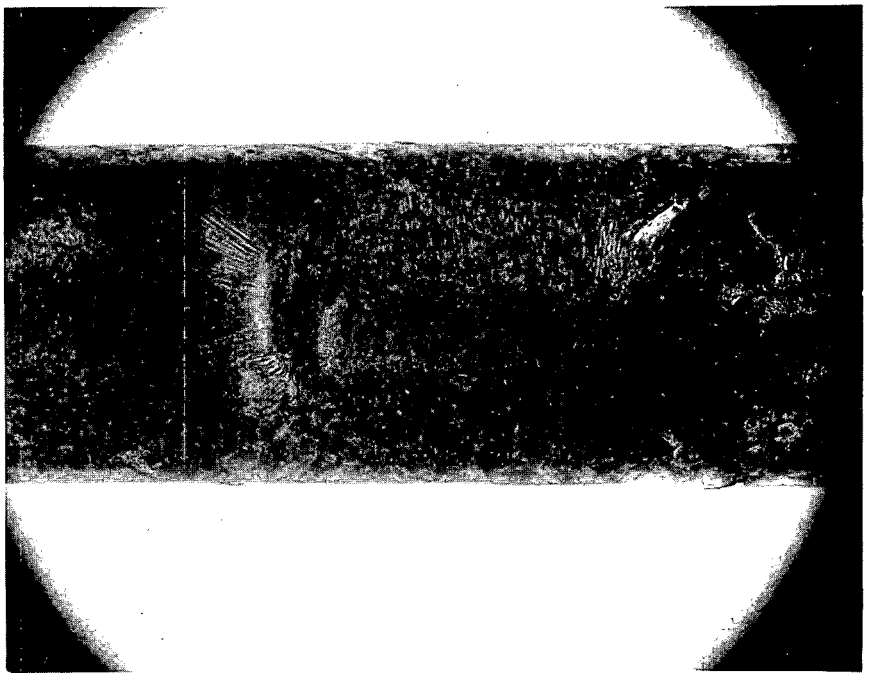

(Mag 2X)

b. Tube 41

7693-4786

Figure A-1. Macrographs of Wastage Areas for Tubes 41 and 42 (Target Tubes)

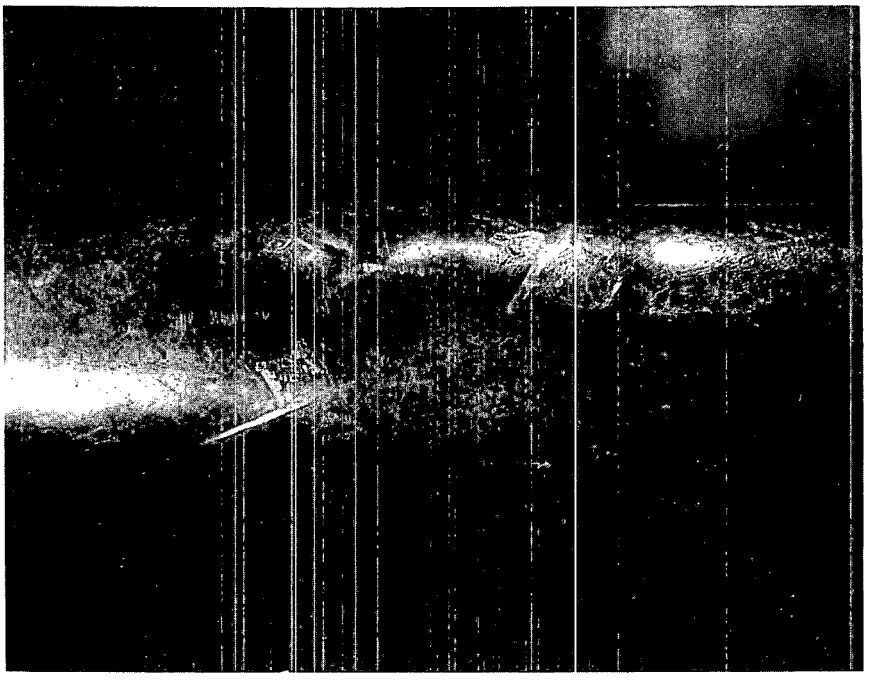

(Mag 3/4X)

a. Tube 44

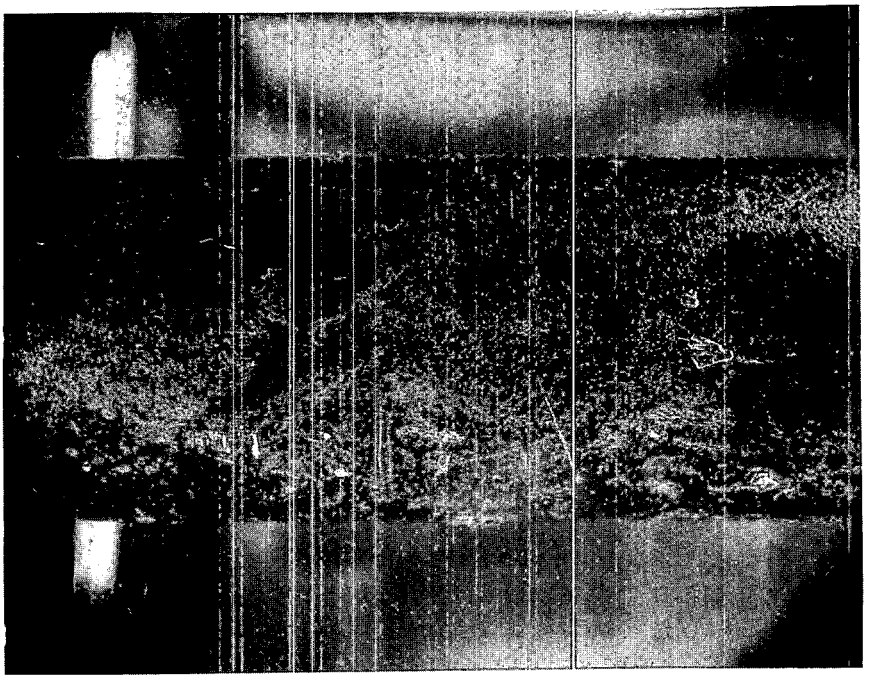

(Mag 2X)

b. Tube 46

7693-4787

Figure A-2. Macrographs of Wastage Areas for Tubes 44 and 46 (Target Tubes)

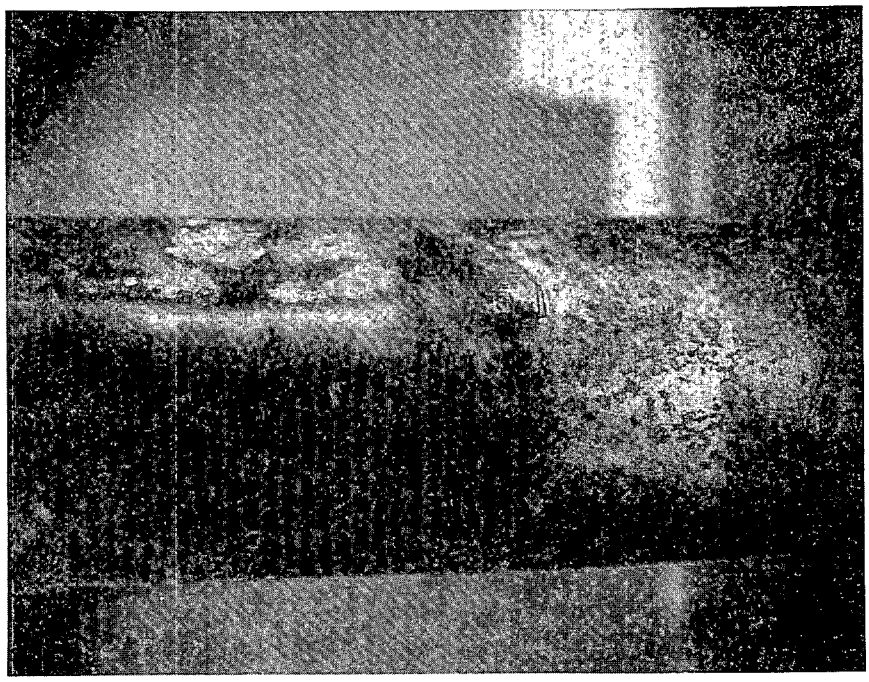

(Mag 2X)

a. Tube 46-A3

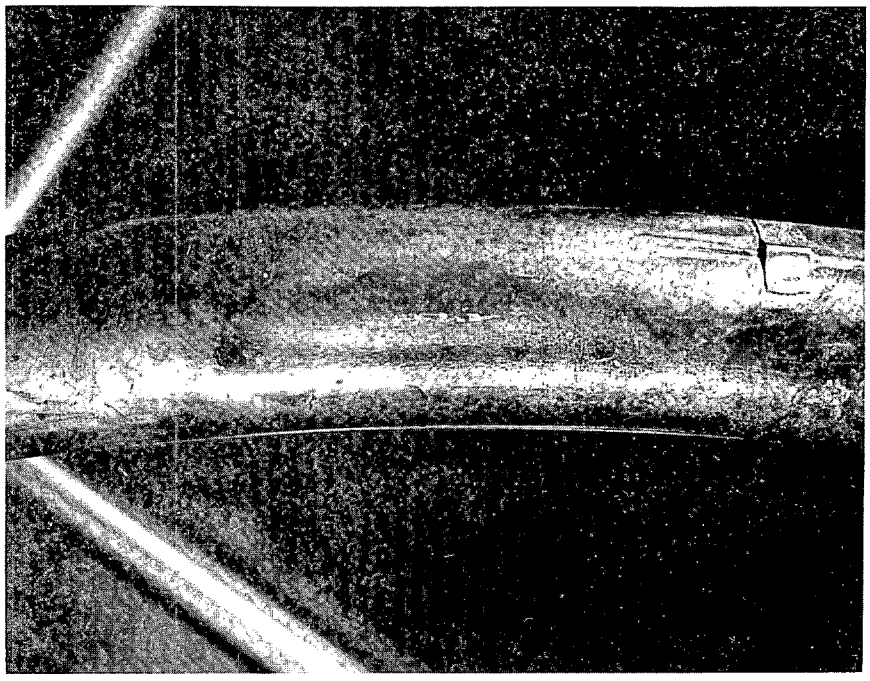

(Mag 3/4X)

b. Tube 46-B3

7693-4788

Figure A-3. Macrographs of Wastage Areas for Tubes 46-A3 and 46-B3 (Secondary Tubes)

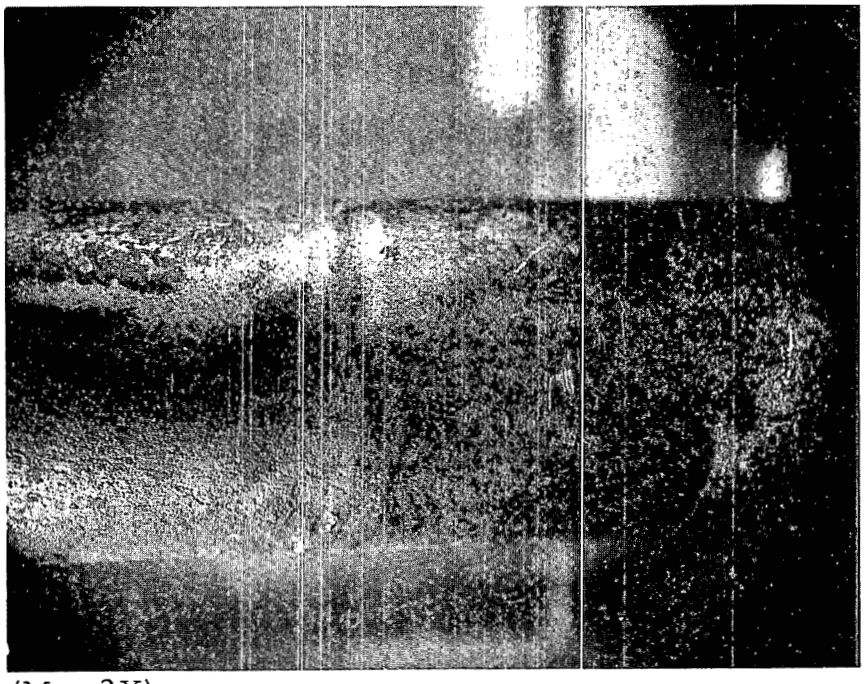

(Mag 2X)

a. Tube 46-B4

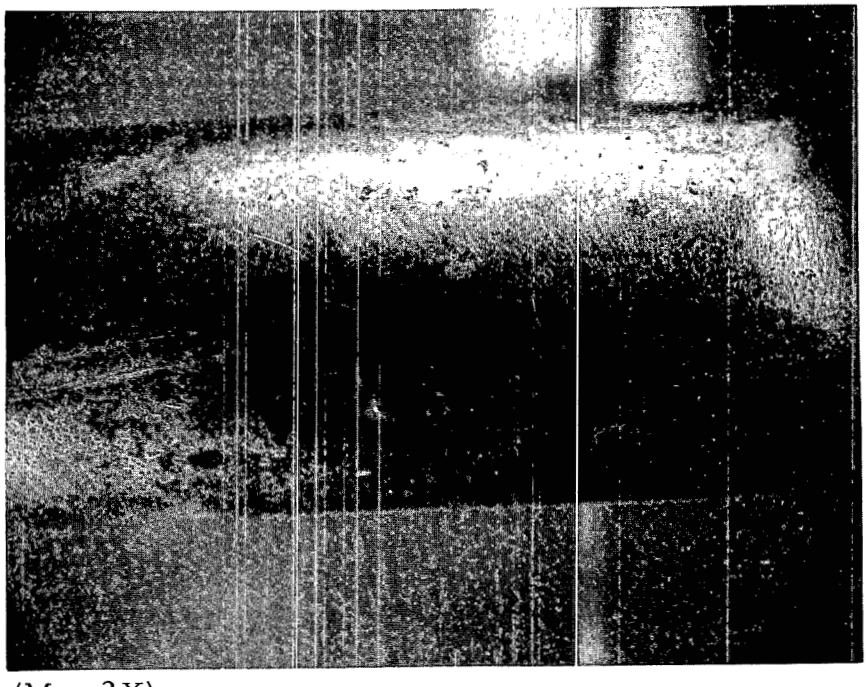

(Mag 2X)

b. Tube 46-B5

7693-4789

Figure A-4. Macrographs of Wastage Areas for Tubes 46-B4 and 46-B5 (Secondary Tubes)

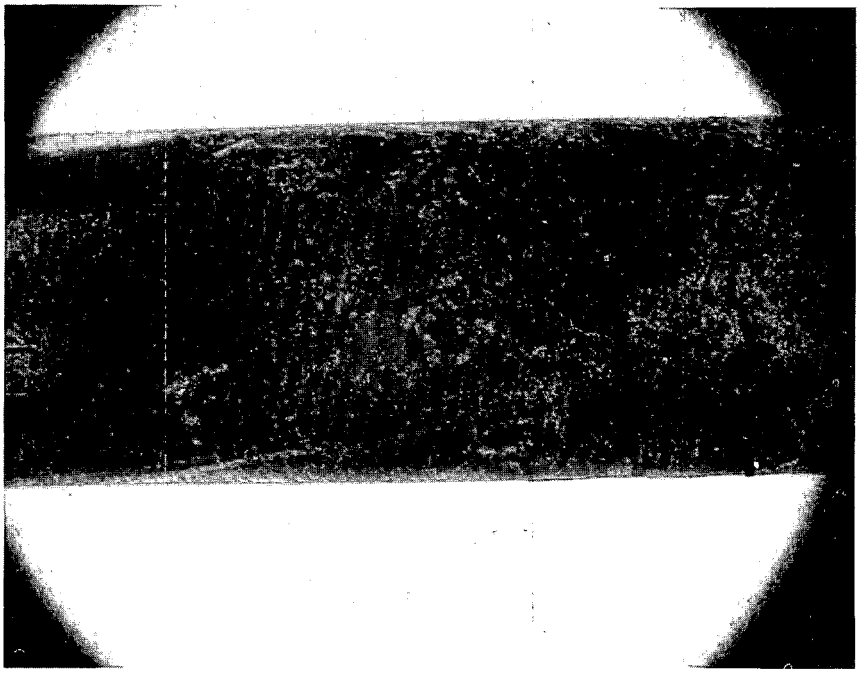

(Mag 2X)

a. Tube 47 (Target Tube)

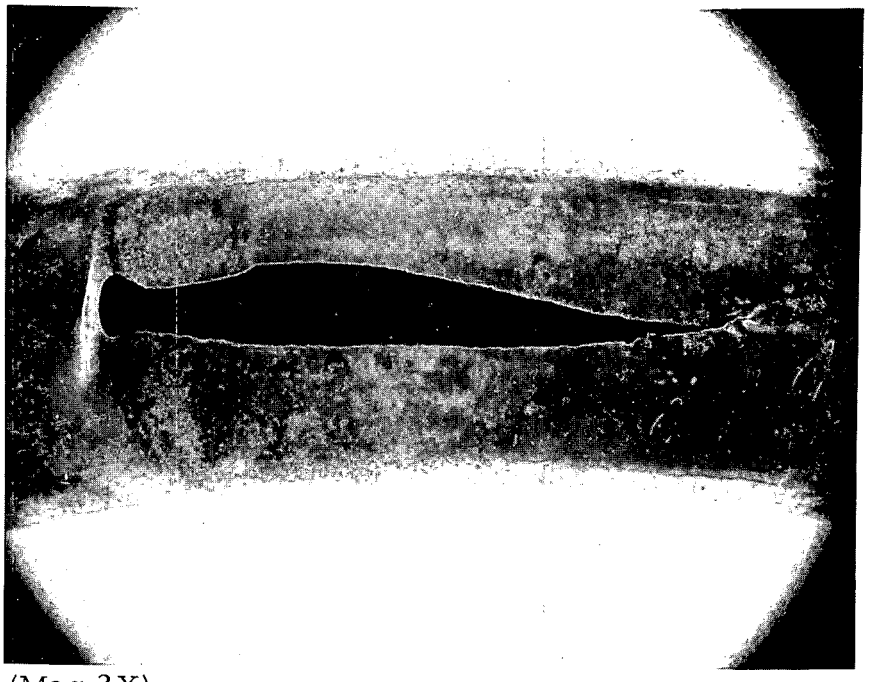

(Mag 2X)

b. Tube 47-A2

7693-4790

Figure A-5. Macrographs of Wastage Areas for Tubes 47 and 47-A2 (Secondary Tube)

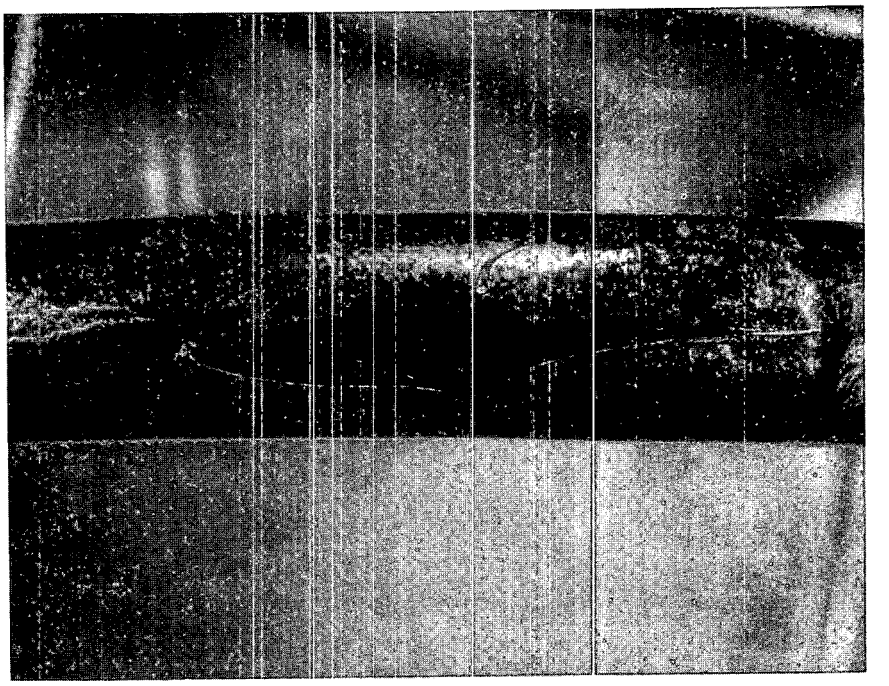

(Mag 1-1/4X)

a. Tube 47-A-3

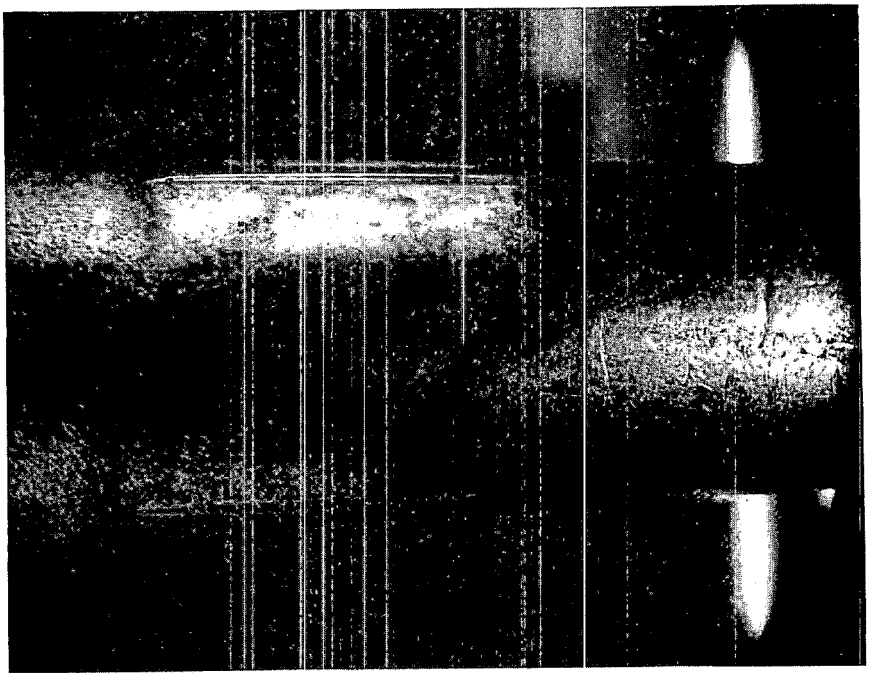

(Mag 2X)

b. Tube 47-B3

7693-4791

Figure A-6. Macrographs of Wastage Areas for Tubes 47-A3 and 47-B3 (Secondary Tubes)

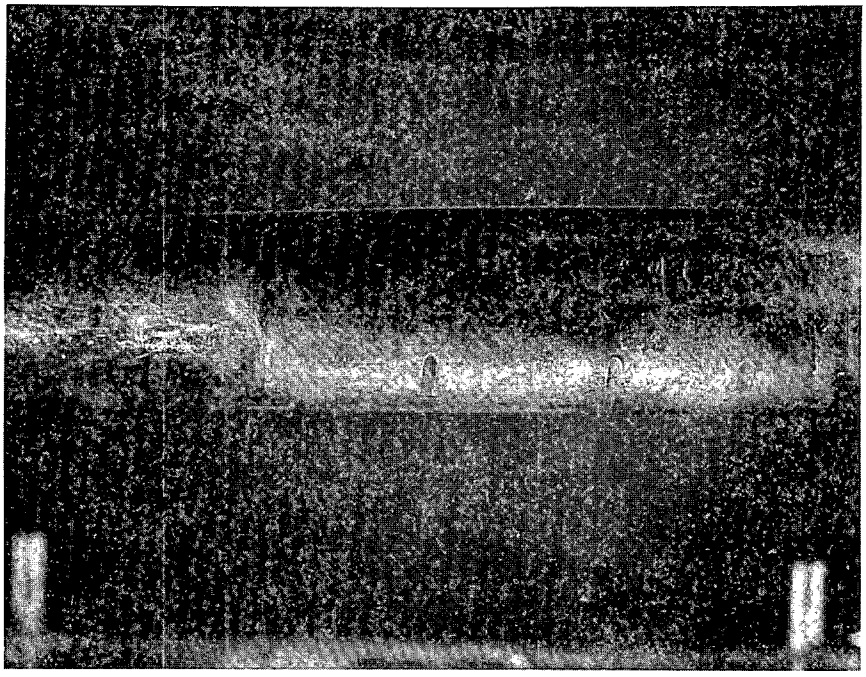

(Mag 1X)

a. Tube 47-B5

(Mag 1X)

b. Tube 47-C5

7693-4792

Figure A-7. Macrographs of Wastage Areas for Tubes 47-B5 and 47-C5 (Secondary Tubes)

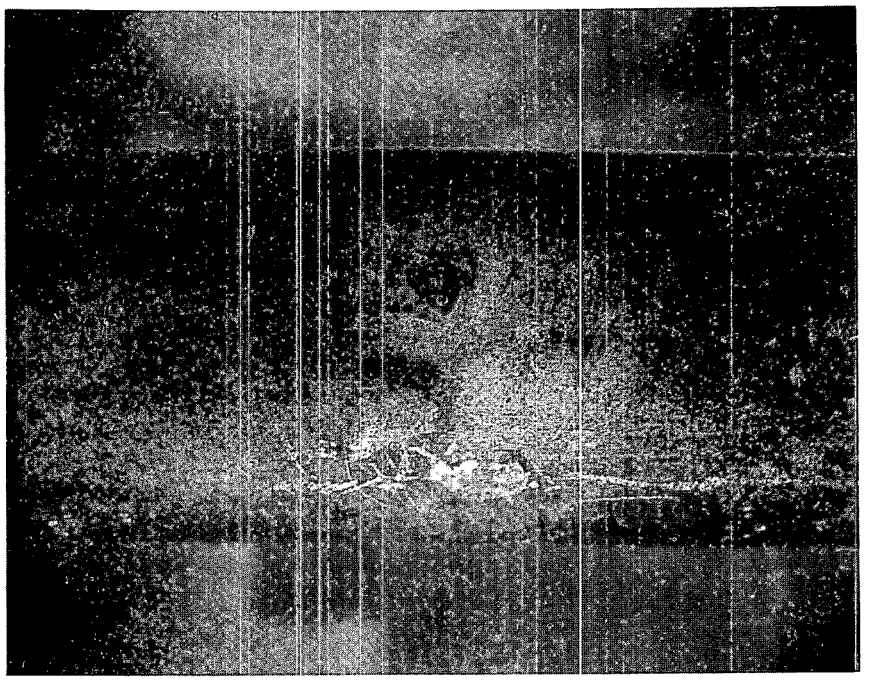

(Mag 2X)

a. Tube 48

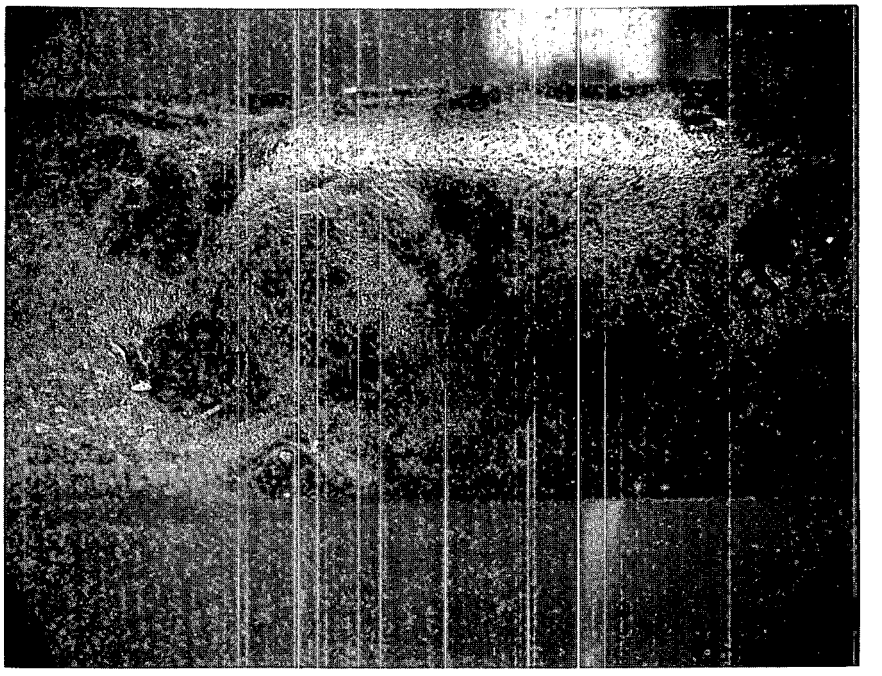

(Mag 2X)

b. Tube 48(b)

7693-4793

Figure A-8. Macrographs of Wastage Areas for Tubes 48 and 48(b) (Target Tubes)

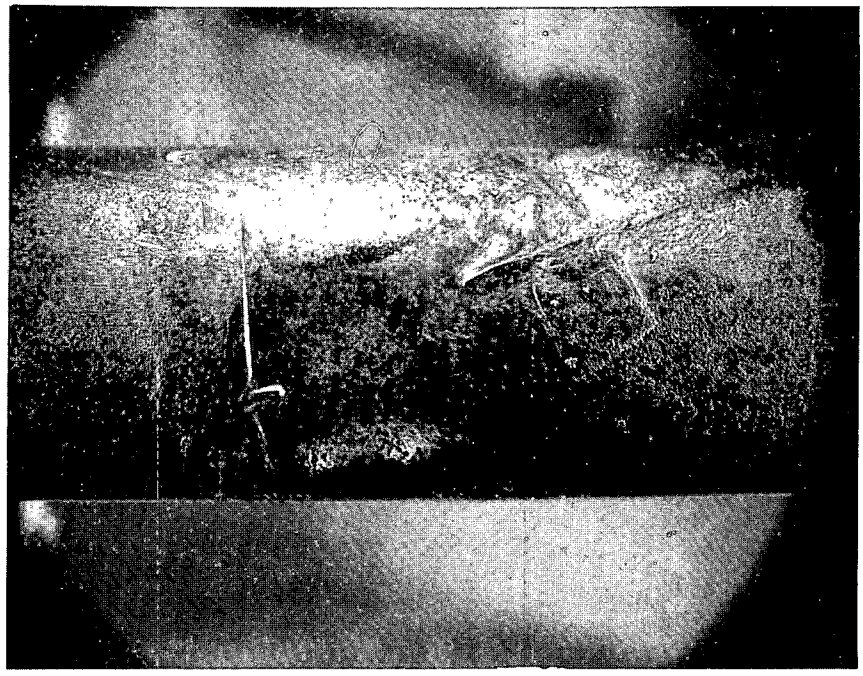

(Mag 2X)

a. Tube 50

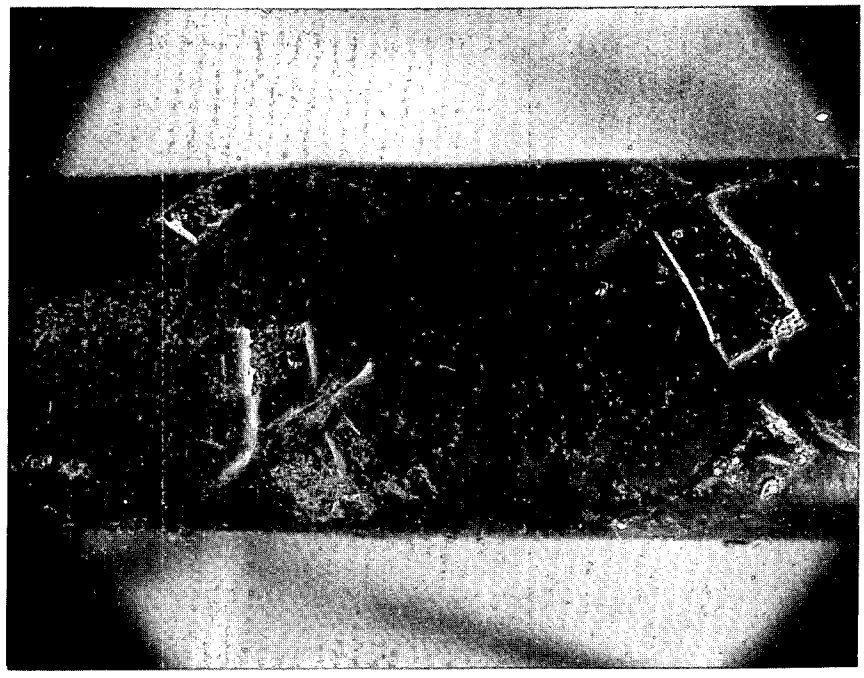

(Mag 2X)

b. Tube 52-B4

7693-4794

Figure A-9. Macrographs of Wastage Areas for Tubes 50 and 52-B4 (Target Tubes)

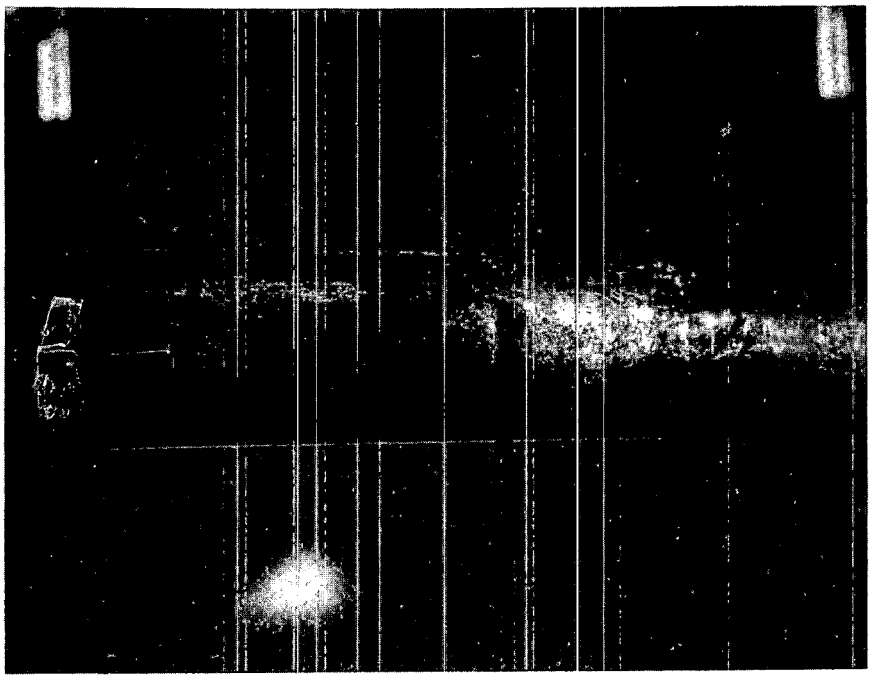

(Mag 1X)

a. Tube 52-A3

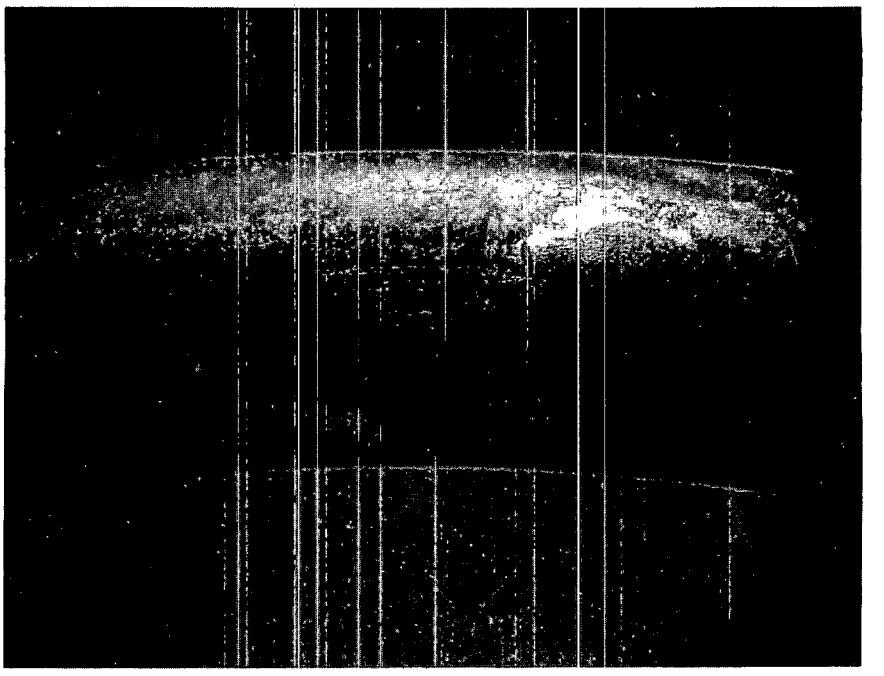

(Mag 2X)

b. Tube 52-A4

7693-4795

Figure A-10. Macrographs of Wastage Areas for Tubes 52-A3 and 52-A4 (Secondary Tubes)

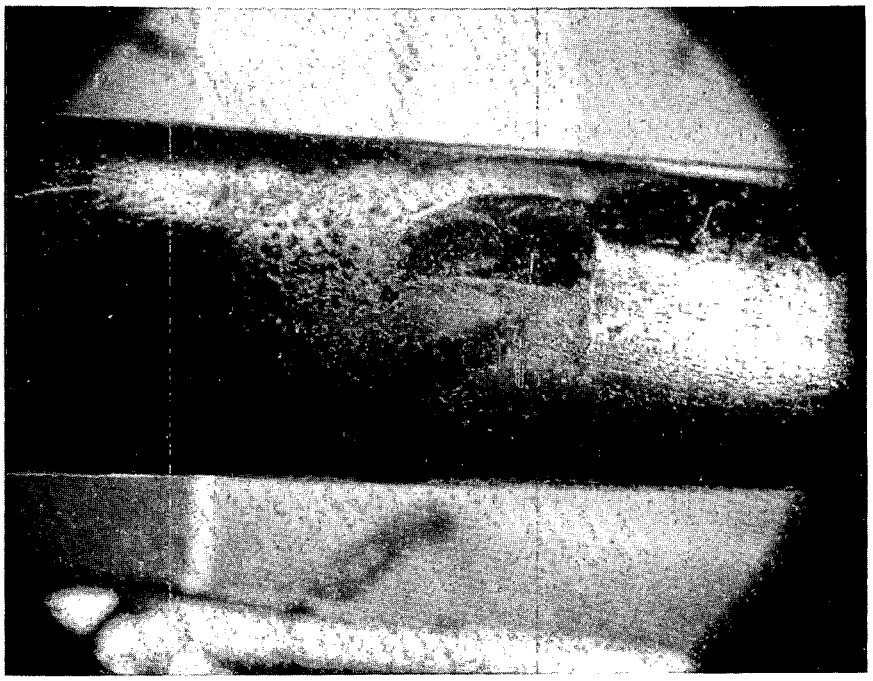

(Mag 2X)

a. Tube 53-B4

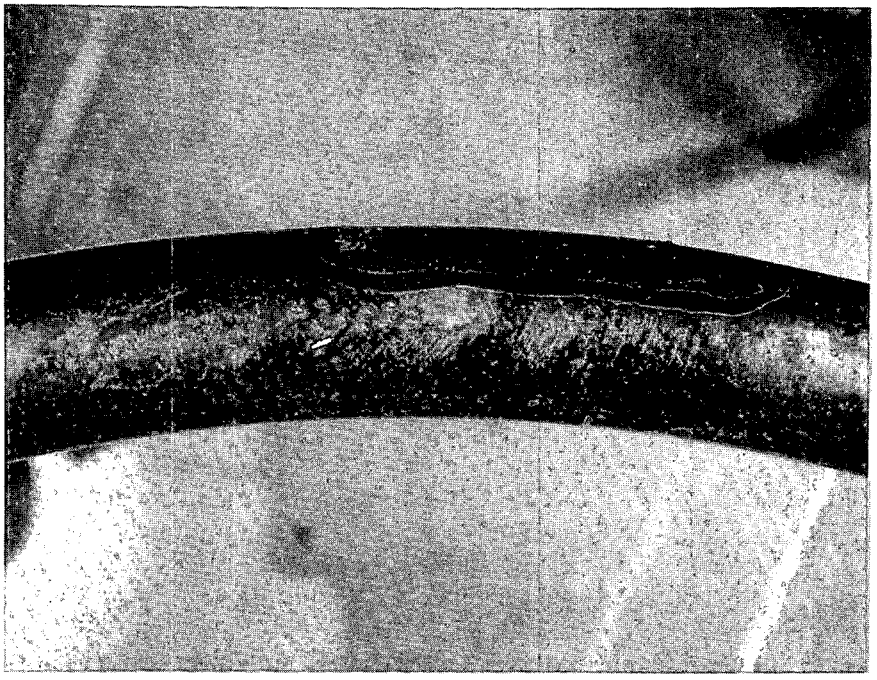

(Mag 1X)

b. Tube 53-A3

7693-4796

Figure A-11. Macrographs of Wastage Areas for Tubes 53-B4 and 53-A3 (Secondary Tubes)

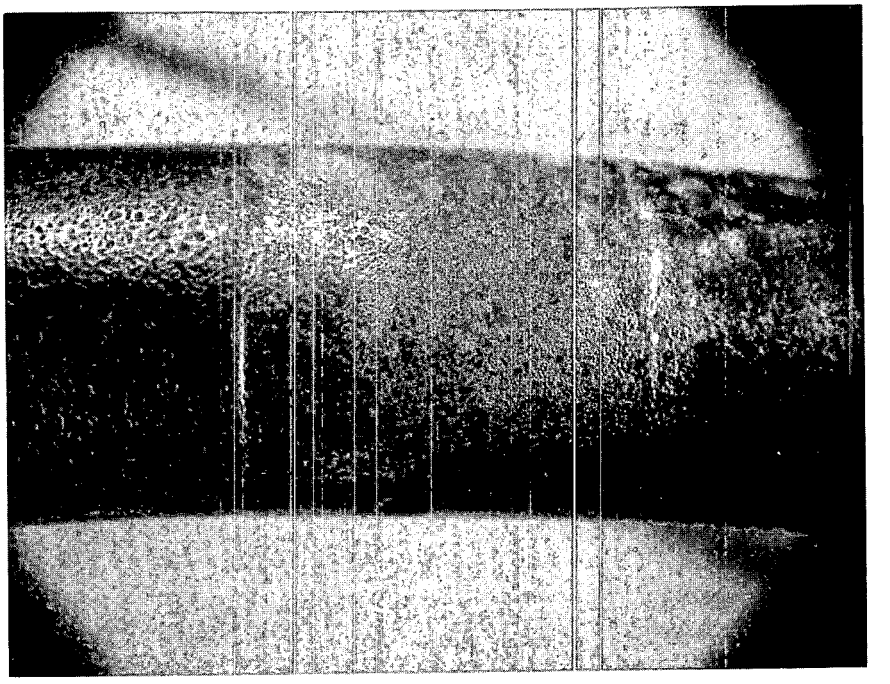

(Mag 2X)

a. Tube 53-A5

(Mag 2X)

b. Tube 53-B5

7693-4797

Figure A-12. Macrographs of Wastage Areas for Tubes 53-A5 and 53-B5 (Secondary Tubes)